



UNIVERSITY OF
CAMBRIDGE
Department of Engineering

Pushing the bounds of energy harvesting

Author Name: Matthew James Bryan

Supervisor: Dr Tore Butlin

Date: 27/05/2024

I hereby declare that, except where specifically indicated, the work submitted herein is my own original work.

Signed

A handwritten signature in black ink that reads "M. Bryan".

Date 27/05/2024

‘Pushing the bounds of energy harvesting’

Part IIB Project

Matt Bryan (**mjb314**)
Magdalene College, University of Cambridge
Supervisor: Dr Tore Butlin, Division C

May 27, 2024

Technical Abstract

Energy harvesting is an expansive academic field, and presents an attractive solution for powering devices. By converting mechanical energy that would otherwise be dissipated into useful electrical energy, supply difficulties associated with applications such as sensors in inaccessible environments can be solved. However, the practical successes of such systems have been limited due to their low power output. As a result, much of the present literature focuses on improving their harvesting performance.

Work by Langley presents a bound on the maximum power that can be harvested by a device subject to broadband base acceleration. The theoretical upper limit on a device’s performance is only proportional to the mass of the system and the spectrum of its input. Therefore, this bound acts as a ceiling for the power output of a harvesting device of a given size.

However, scope for improvement exists in the interrogation of the underlying assumptions of the bound, the most promising of which is the inclusion of rotational input alongside the translational input dictated by the bound. Whilst this modification does not lead to the bound being exceeded, this circumvention has the potential to improve the performance of a given device. This project focused on the field of implantable medical devices (IMDs), which are often difficult to access and located at sites which undergo significant rotational motion. Therefore, significant improvements in harvester power output would be invaluable for this application.

To validate this hypothesis, a system subjected to both translational and rotational input was modelled, and its behaviour characterised with a practical realisation alongside a numerical model. A piezoelectric bending transducer was used to create a single-degree-of-freedom harvester, connected to a base which provided either translational (Type A), rotational (Type B) or a combined (Type C) input. The design of the rig was iterated in order to ensure that the modes were decoupled, and instrumented with accelerometers to determine the transfer function of the harvester alone with respect to the three input types.

Practical experiments for varying amplitude showed the system was approximately linear, and resistance varying experiments showed that the device exhibited power matching in its harvesting. The power output for each of the input types was then compared, showing the potential for the rotational input to improve performance.

The results of the experimental work were then incorporated into both a time-domain and frequency-domain model of the system, which showed good agreement in predicting the performance of the system. These models were then developed into a multi-degree-of-freedom case using a periodic structure form, and the validity of scaling to a given application was explored.

Purely rotational systems were shown to have good harvesting performance for a given input when compared to their translational equivalent, however results from the representative combined input showed a decrease in performance. The composition and phase of the input components was suggested as a reason, and characterising these parameters in relation to the device performance would be a valuable result of future work.

To Roger, my late grandfather, from whom I learned so much.

Acknowledgements

I would like to give my utmost thanks to my supervisor Dr Tore Butlin for his enthusiasm, support, and guidance this year; his kindness and expertise have been invaluable in turning a very open question into a highly enjoyable project. I would also like to acknowledge Prof. Ashwin Seshia for his advice on piezoelectric transducers, and Stefan Savage and the workshop technicians for their help in the construction of the experimental rig.

I would also like to express my gratitude to Dr Richard Roebuck for his unwavering support and encouragement throughout my four years at Magdalene. Also, to the members of the Dynamics and Vibration Research Group, and my friend Max Langtry, who have provided a supportive environment at CUED and helped develop my passion for research.

Finally, I would like to thank my friends and family for their support in all my endeavours and for being there in difficult times. Particularly my parents, who have always encouraged me to pursue my interests, and without whom I would not be where I am today.

Contents

1	Introduction	3
1.1	MOTIVATION	3
1.2	OBJECTIVES	4
2	Background theory	5
2.1	ENERGY HARVESTING	5
2.2	ANGLEY'S BOUND	6
2.3	CIRCUMVENTING THE BOUND	8
2.3.1	NONLINEAR SYSTEMS	8
2.3.2	EXCITATION METHODS	9
2.3.3	ROTATIONAL SYSTEMS	9
2.4	ENERGY HARVESTING APPLICATIONS	10
2.4.1	CLASS-BASED DESIGN	10
2.4.2	IMPLANTABLE MEDICAL DEVICES (IMDs)	11
3	System modelling	13
3.1	ENERGY HARVESTER ARCHITECTURE	13
3.2	SIMPLIFIED CANTILEVER MODEL	14
3.3	PERIODIC STRUCTURE MODEL	15
3.4	SCALING FOR THE USE CASE	18
4	Experimental work	19
4.1	METHODOLOGY	19
4.2	TEST RIG DESIGN	19
4.3	EQUIPMENT	22
4.3.1	PIEZOELECTRIC COMPONENT	22
4.3.2	INSTRUMENTATION AND DATA ACQUISITION	23
4.4	TRANSLATIONAL, ROTATIONAL, AND COMBINED INPUTS	24
4.5	SYSTEM CHARACTERISATION	27
4.6	AMPLITUDE EXPERIMENTS	30
4.7	HARVESTING EXPERIMENTS	33
5	Simulation work	37
5.1	SINGLE-DEGREE-OF-FREEDOM SYSTEMS	37
5.2	MULTI-DEGREE-OF-FREEDOM SYSTEMS	39
5.3	TIME AND FREQUENCY DOMAIN COMPARISON	39
6	Model verification	40
6.1	PIEZOELECTRIC CALIBRATION	40
6.2	PARAMETER FITTING	42
6.3	COMPARISON OF SIMULATED AND EXPERIMENTAL RESULTS	44
7	Conclusions	47
7.1	RECOMMENDATIONS FOR FUTURE WORK	48
8	References	49
A	Risk assessment retrospective	50

1 Introduction

1.1 Motivation

Much of the engineered world is reliant on systems that require power to function, and many of these systems undergo mechanical vibration in operation, whether intentional or undesirable. Therefore, the concept of converting this vibrational energy into useful electrical energy is an attractive one for applications which exist in that overlap. The field of energy harvesting has grown significantly in recent years, initially motivated by powering devices in difficult to access environments, but now work is being done to power a range of devices from sensors to biomedical implants.

Despite the growth of the field, such devices have seen little commercial success or widespread adoption. The primary reason for this is the low power output of energy harvesting devices, which limits their use to a small number of low power applications. Therefore, there is significant scope for improving their performance which would allow for a greater number of successful applications.

A theoretical framework for the performance of energy harvesting devices is provided by Langley [1]: that the power output of a system is limited only by its mass and the spectrum of its input. This bound is a theoretical upper limit on the performance of a system subject to broadband base acceleration, and so the question arises as to whether careful interrogation of the underlying assumptions could improve performance.

The aim of the project was not to ‘break’ the bound, but to instead explore methods by which a practical system might advantageously ‘circumvent’ its conditions: such methods include modifying the spectrum or type of input. Such methods can be tailored to a specific application, for example where the input is known to deviate from the assumption of broadband white noise, and so performance might be improved in a more specific case.

Having identified the most promising method of circumvention as the use of a rotational input, the project aimed to determine the performance of a harvesting system both numerically and practically. By starting with a simple single-degree-of-freedom experimental rig, the potential benefit of including a rotational input compared to sole translation was explored. From this, a numerical model of a multi-degree-of-freedom system was developed, employing a number of arguments to scale the results to a practical system.

Therefore, the final aim of the project was a validated numerical model to aid the design of multi-degree-of-freedom rotational energy harvesters which showed a performance increase over a solely translational system. Such a model would be of significant benefit to the field of energy harvesting, especially considering the large number of parameters in their design, and the wide range of applications for which they are suitable. A successful model could inform the use of improved energy harvesting devices for a whole new range of applications.

1.2 Objectives

The project began with the broad aim of ‘pushing the bounds of energy harvesting’, with the intention of exploring cases not covered by Langley’s bound. Therefore the initial objectives of the project were to:

- Investigate the theoretical framework of Langley’s bound, and identify the methods by which it might be ‘circumvented’ to increase harvester performance.
- Review the energy harvesting literature to assess the feasibility of the candidate methods identified.
- Determine the most promising method of bound circumvention in the context of the project, and formulate a list of objectives to verify its effectiveness.

Following this, it was decided that rotational was the candidate method that showed the most promise for improving the performance of an energy harvesting system. With this new, more detailed focus, the objectives of the project were formalised as:

1. Formulate a theoretical model for a system subject to both translational and rotational input, and identify a class of applications and a dimensional scale for which it might prove beneficial.
2. Design and manufacture a practical rig to experimentally test the performance of rotational and translational inputs on a single-degree-of-freedom harvesting system.
3. Create a numerical model of the practical system, and determine a method for scaling the results to a multi-degree-of-freedom system.
4. Use the experimental results to inform the numerical model, and validate its predictions for a real system.
5. Show that a rotational input can increase the performance of an energy harvesting system over a solely translational input.

2 Background theory

2.1 Energy harvesting

Energy harvesting describes the process whereby a system transduces ambient energy into a more useful form which can then be used to power a device. Most commonly, this is the conversion of mechanical energy into electrical energy, but other forms of energy can be harvested depending on the type of transducer.

The academic field of energy harvesting has grown significantly in recent years, yet very few devices have been commercially successful for a number of reasons. The primary reason is that the power output of such devices is low and often insufficient to supply all but the least taxing of devices. This is partly due to the amount of power available in ambient sources, but also because of the low transduction efficiency of harvesting devices. This means that there is still scope to improve the performance of such devices, which would result in a greater number of applications for which they are suitable.

The literature on energy harvesting is vast, with almost 10,000 publications in 2022, but can be broadly categorised into four areas: transduction, design, applications, and advances.

The major transduction methods for vibrational energy harvesting in the literature are piezoelectric, electromagnetic, electrostatic, and triboelectric [2], each with their own advantages and disadvantages. Triboelectric transducers have a high conversion efficiency, but their configuration is unsuitable for the vast majority of applications. Electrostatic transducers can be damaged by off-axial vibrations, limiting their use cases. Therefore, piezoelectric and electromagnetic transducers are the most commonly used, but the choice of transduction method is highly dependent on the application of the device. Piezoelectric transducers are better suited to micro-scale devices as electromagnetic transducers are limited by the scale of their mechanism.

Energy harvester design is also well explored in the literature, with a number of different configurations and methods for improving their performance. Design is highly dependent on the use case, but many devices are tailored to their respective input types. One example of note is an up-converting system with a rotating proof mass to harvest energy from low frequency walking vibrations, converting them to a higher frequency to match the resonance of a piezoelectric transduction cantilever [3]. Therefore, it is evident that careful design offers a significant opportunity for improving the performance of energy harvesting devices.

The applications of energy harvesting devices are vast, but the most common are in structural health monitoring [4], wearable devices, and, increasingly, biomedical devices [5]. Each application has varying requirements on the power outputs required and the scale and constraints of the device itself.

Finally, a number of advances in device performance have been made in recent years. An example of which is the harnessing of nonlinearity, which has been shown to improve the performance of energy harvesting devices [6], especially with bistable systems. Additionally, energy harvesting devices are being implemented at smaller and smaller scales, and optimised in MEMS devices as an efficient power source [7].

With so many potential configurations, transduction methods, and applications, the

design of an energy harvesting system is a complex task. Therefore, it is invaluable to have a theoretical framework for the performance of such a device, such as an upper bound on the power it can harvest.

2.2 Langley's bound

The initial concept of this project arose from Langley's 2014 paper, '*A general mass law for broadband energy harvesting*' [1], in which a bound is derived for the power dissipated by a general system that is only a function of the system's mass and the input power spectral density.

The bound states that '*the total power absorbed by a linear or nonlinear multi-degree-of-freedom electromechanical system subjected to white noise base acceleration depends only on the spectral density of the base acceleration and the total mass of the system*'. Set in the context of energy harvesting, this statement quantifies a theoretical upper limit on the power that can be harvested from a given input.

A general linear or nonlinear system with a total mass M_T is described and subjected to an input, $x(t)$, with power spectral density S_0 . The resulting output, $y(t)$, can then be used to find the power dissipated by the system ($P_D = C(\dot{y} - \dot{x})^2$ for a simple single-degree-of-freedom case).

$$\mathbb{E}[P_D] \leq \frac{\pi}{2} S_0 M_T \quad (1)$$

Langley's result states the simple relationship that the expectation of the power dissipated by the system is less than or equal to the product of S_0 , M_T , and a constant, $\frac{\pi}{2}$ defined by the double-sided power spectral density of the output $S_{yy}(\omega)$ as shown in Equation 1.

Langley presents a number of methods for proving this for a general case [1], but the result can be shown to hold for a simple single-degree-of-freedom system subject to base acceleration.

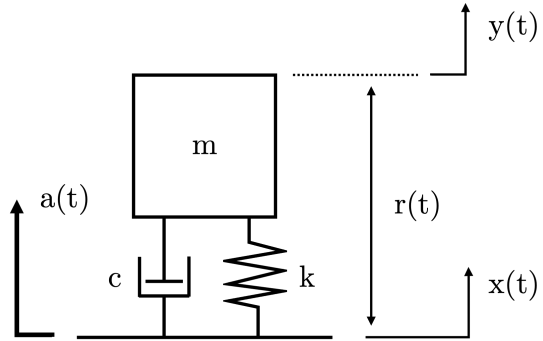


Figure 1: A simple single-degree-of-freedom system with a mass m , damping c , and stiffness k subject to a base acceleration $a(t)$ equal to $\ddot{x}(t)$.

Figure 1 shows a simple single-degree-of-freedom system subject to base acceleration a , with the displacement of the base given by x and the absolute response of the system by

y . This results in a relative variable $r = y - x$ which can be used to describe the system, giving the equation of motion in either form:

$$m\ddot{y} + c(\dot{y} - \dot{x}) + k(y - x) = 0 \quad (2)$$

$$m\ddot{r} + cr + kr = -m\ddot{x} = -ma \quad (3)$$

Taking the Laplace transform of Equation 3 in terms of the variable $s = i\omega$ gives:

$$ms^2\bar{r}(s) + cs\bar{r}(s) + k\bar{r}(s) = -m\bar{a}(s) \quad (4)$$

which then yields the transfer function of the system from the input acceleration to the relative displacement:

$$H(s) = \frac{\bar{r}(s)}{\bar{a}(s)} = \frac{-m}{ms^2 + cs + k} \implies H(i\omega) = \frac{-m}{k - m\omega^2 + i\omega c} \quad (5)$$

For a broadband acceleration input where $S_{aa}(\omega) = S_0$, the power spectral density of the output is given by $S_{rr}(\omega) = |H(i\omega)|^2 S_{aa}(\omega)$, and the integral of the PSD gives the RMS squared relative displacement. For the RMS squared relative velocity, this is found by first multiplying the transfer function by $i\omega$:

$$\sigma_r^2 = \int_{-\infty}^{\infty} |i\omega H(i\omega)|^2 d\omega = \int_{-\infty}^{\infty} \frac{m^2\omega^2}{(k - m\omega^2)^2 + \omega^2c^2} d\omega \quad (6)$$

Solving the integral in Equation 6 (using a standard result provided by Newland [8] via the residue theorem) gives:

$$\sigma_r^2 = \frac{\pi}{2cm} (m^2 S_{aa}(\omega_n)) = \frac{\pi}{2c} (mS_0) \quad (7)$$

and the expected power dissipated by the system is given by:

$$\mathbb{E}[P_D] = c\sigma_r^2 = \frac{\pi}{2} S_0 m = \frac{\pi}{2} S_0 M_T \quad (8)$$

Equation 8 is the result derived by Langley, applied here to give the upper bound on the power dissipated by a linear single-degree-of-freedom system subject to broadband base acceleration. Langley subsequently proved the same result for a more general system, with history-dependent nonlinearities and non-white noise excitation in 2015 [9].

This bound in the context of energy harvesting serves as the upper limit on the performance of such a system, that the maximum harvested power is dependent on the mass of the device. Such a constraint is a theoretical limit dependent on the mass, which if thought of in terms of practical size, states a performance limit for a given scale of device. The project is therefore motivated by the question of whether this bound can be circumvented by careful interrogation of its underlying assumptions to create devices that can provide higher power outputs.

2.3 Circumventing the bound

Having established Langley's bound as a theoretical limit on the performance of a system, the question arises as to whether this bound can be improved upon using methods outside of the scope of Langley's work. Such a method might allow the bound to be 'circumvented': not explicitly broken, but detail how a practical system might be altered to allow for a performance increase that is closer to the bound.

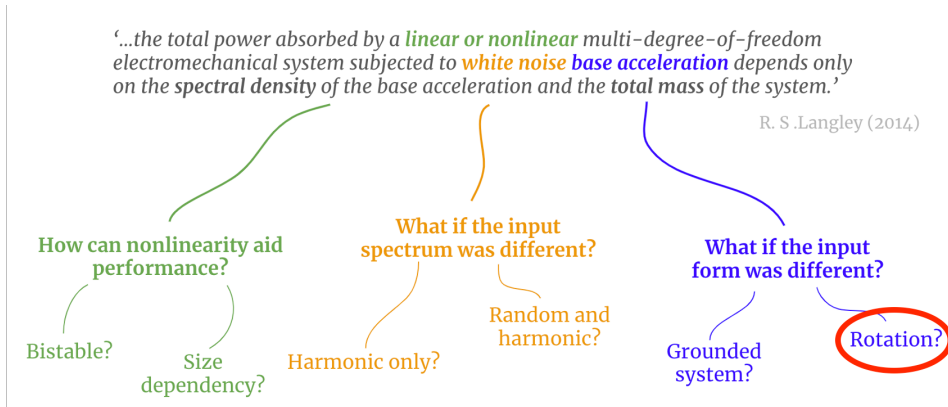


Figure 2: A visual summary of the methods by which Langley's bound might be circumvented to increase the performance of a theoretical energy harvesting system.

Figure 2 presents a visual summary of the methods explored during the project that had potential to circumvent Langley's bound for the described conditions of 'white noise base acceleration'. These methods can be categorised into three groups: design of nonlinear systems, modification of the input spectrum, and modification of the input form.

Having assessed the potential for each of these methods to improve the performance of a system alongside the ease of achieving them, both numerically and practically, it was decided that the project would focus on the rotational input question posed in Section 2.3.3.

2.3.1 Nonlinear systems

Exploiting the nonlinear behaviour of a system can allow for a performance improvement over a linear system, and such types of energy harvesters have been well explored in the literature. Whilst these systems do not break the bound, a number have been demonstrated to offer a performance increase over their linear counterparts [6].

The major method of exploiting nonlinearity is through the use of bistability, whereby the system has two stable states; one method of achieving this is by the addition of a magnet to a cantilever tip. The benefit of nonlinearity is a wider bandwidth of operation, which when subject to a comparatively broadband excitation, allows for a larger output power from the harvester. Another benefit is that of 'frequency up-conversion', whereby the system can convert a low frequency input to a higher frequency output, which can then be more efficiently harvested by a piezoelectric transducer [3]. This helps to alleviate issues of scale when the natural frequency of the device, dictated by its mass and stiffness, is much higher than the vibrational source.

While nonlinear harvesting systems can offer such benefits, their analysis is often complex, and the fabrication and verification of a practical system is difficult. Therefore, the project did not pursue this method further.

2.3.2 Excitation methods

As stated in Langley's bound, the spectrum of the input and its type are important factors for performance. The bound is derived for a system subject to white noise base acceleration, but one subject to a harmonic input might offer a higher power output.

If a given system with zero damping is subject to a harmonic input at its natural frequency, the output displacement, velocity, and acceleration are theoretically infinite. This in turn suggests that the power output of the system is also infinite. However, such a model does not consider the practical ramifications: an infinite output displacement would need a system with infinite dimensions, and some degree of damping in the system is unavoidable, and is required to harvest energy. However, this suggests that tailoring to the input might offer a performance increase over the broadband case at the cost of generality.

Another issue is that of tuning a harmonic system to a specific frequency. If the frequency of the input and the system are not exactly equal, then the performance of the device is severely diminished, so a practical system would need a wider working range of frequencies to be practically effective.

Therefore, the suggestion of a harmonic system with probabilistic properties was made. Such an input has a non-zero probability density between two frequencies, so the exact input frequency is not known, but rather the system is tuned to this range of frequencies. Taking an ensemble of these cases leads to a narrowband white noise input, which is physically realisable unlike a true white noise input. Therefore, this type input will be used in numerical and practical work to determine the performance of the system.

An additional consideration was in relation to the 'base acceleration' of the system. If instead one of the degrees of freedom of the system was 'grounded', that is connected to a far larger mass, then the performance might be improved by the increase in M_T , the total effective mass. A physical representation of this would be a damper attached from a bridge deck to the ground, as seen in the retrofitting of London's Millennium Bridge [10]. However, designing a lab based system to test this would be difficult and subject to a number of practical limitations, and so this method was not pursued further.

2.3.3 Rotational systems

Langley's bound is presented in the form of a translational input, but is generalisable for any form of input coordinate. If instead the bound was re-expressed for a rotational base acceleration, $\ddot{\theta}$, then the limit might instead be proportional to the spectrum of the input and effective moment of inertia of the system, I_T .

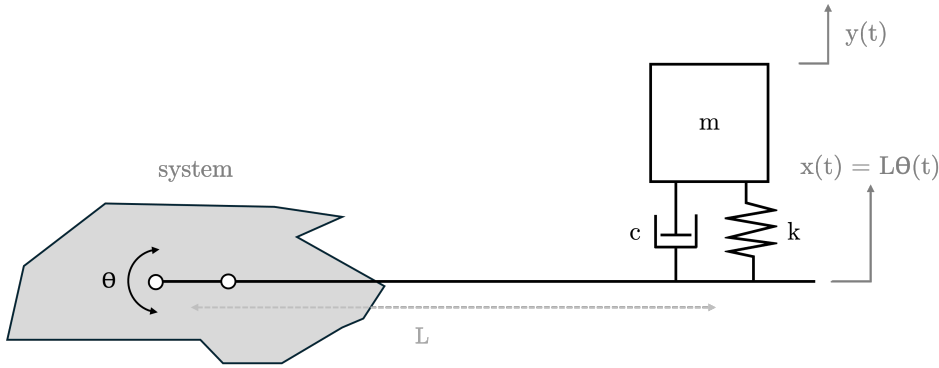


Figure 3: A theoretical rotational system comprising of a single-degree-of-freedom harvester as in Figure 1 connected to an arbitrary system by a rigid rod of length L , resulting in a case governed by an inertia limit.

Figure 3 shows a theoretical system comprising of a single-degree-of-freedom energy harvesting device as detailed in Figure 1 connected to an arbitrary system by a rigid rod of length L with some rotational input θ . By considering that the rod could be extended indefinitely, and that $I_T = M_T L^2$, the inertia bound could be arbitrarily increased over the equivalent mass bound.

Such a system is still subject to practical limitations on the size of the harvester and the spectrum of the input. However, for a given size or set of dimensional constraints, it is possible that a rotational input might allow for a performance increase over a translational input. This is the question that the project aims to answer, supported by experimental and simulation work of such systems.

2.4 Energy harvesting applications

2.4.1 Class-based design

Section 2.3 discusses a number of methods by which Langley's bound might be circumvented, before focusing on the rotational input question. Such methods are highly theoretical however, making them difficult to compare in a practical sense. Whilst the performance of a device might be scaled by a system parameter like mass or size, this leads to another question: what order of magnitude of system should be used for comparison?

In order to make comparisons between different energy harvesting systems more useful, a class-based design framework can be used. The power output per volume is used as a performance metric rather than the absolute power output: this allows for a comparison between systems of different sizes, and easier comparison with Langley's bound, which is in terms of the effective device mass, M_T .

Then, deciding on an approximate scale, for example, a length between 10^{-3} and 10^{-2} metres, allows for flexibility of system design, whilst still governing the performance of the system relative to its size. Such a framework is determined by the use case, but also dictates the transduction method used, as many perform poorly at smaller or larger scales [2]. In the example region, piezoelectric systems are well suited.

2.4.2 Implantable medical devices (IMDs)

A class-based framework also lends itself well to a particular application. The use of energy harvesting devices in structural health monitoring applications is well established [4], particularly for sensing devices in environments that make maintenance or a wired power supply difficult. A harvesting device can scavenge energy from ambient vibration of the structure to power a sensor to monitor the health of that same structure. Sensors typically have a low power requirement, so the size and performance of the harvesting device is rarely a limiting factor.

Another similar case in which devices must be powered but are often inaccessible is that of implantable medical devices (IMDs), and energy harvesting systems for numerous biomedical applications are increasingly being explored [5]. Such devices can serve a range of purposes, from powering pacemakers to sensors that monitor the health of the body. The power requirements of such devices can vary widely, from the μW range for bone growth stimulators to the W range for total artificial hearts.

Table 1: A table of common IMDs and their power requirements, location within the body, and practicalities of implementation [5].

IMD	Power Req.	Location	Practicalities
<i>Bone growth stimulator</i>	5 - 20 μW	Fractured bone	Small, conformal site
<i>Cardiac pacemaker</i>	< 100 μW	R. ventricle/atrium	Flexible site,
<i>Drug pump</i>	100 μW - 2 mW	Desired site	reasonable power
<i>Body area network</i>	100 μW - 5 mW	Desired site	requirement
<i>Cochlear implant</i>	600 μW - 40 mW	Inner ear	Difficult sites,
<i>Retinal stimulator</i>	1 mW - 100 mW	Retina surface	high power
<i>Total artificial heart</i>	5 - 30 W	Left ventricle	requirement

Table 1 shows a range of common IMDs and their power requirements, locations, and discussion of their practicalities, derived from a review work by Roy et al. [5] on powering solutions for biomedical implants. The table shows that there are significant differences in the power requirements of common IMDs, and that the location of the device can have a significant impact on the ease of implementation.

Bone growth stimulators are typically used to stimulate the growth of bone at a fracture site, and require a very low power input, but such devices must be small and fit close to the surface of the bone. Their conformal shape essentially renders them two-dimensional, leaving little scope for the design of a harvesting device, and so this application would severely limit the success of the project.

Cochlear implants and *retinal stimulators* are used to improve hearing and sight respectively, and are located in the inner ear and on the retina surface. These devices have higher power requirements, and are located in difficult sites, making the design of a harvesting device more challenging. Finally, *total artificial hearts* are used to replace the function of a failing natural heart, and have a high power requirement. The location of the device is less of a concern, but the power requirement is a significant challenge for

the design of a harvesting device that would fit within the body. Therefore these higher power devices were not considered for the project.

Cardiac pacemakers are used to regulate the heartbeat of a patient, and are typically located in the right ventricle or atrium. The power requirements of such devices are low, but the site is relatively flexible, as long as the contact with the heart is maintained. Along with *drug pumps* (which deliver medication to the patient over a prescribed period) and *body area networks* (which are a general network of body sensing devices), these devices offer more flexibility in the design of a harvesting device situated in the body. Therefore, there is more potential for a translational and rotational device to show an improvement, so these devices were chosen as the focus of the project. This choice sets the scale of the device and the desired performance, helping to guide the design of the system.

An energy harvesting system is particularly suited to a *cardiac pacemaker* as the power requirement is low, and the site is relatively flexible, and indeed work has been done to design such a system in the literature [11]. Pacemaker batteries are typically replaced every 8 - 10 years, and so a harvesting device that could extend the life of the battery and reduce the need for surgery would be of significant benefit. The heartbeat acts as the input, typically between 60 - 180 beats per minute or 1 - 3 Hz, giving rise to a potential operating band for a harvesting device.

The biomedical setting of such a device also has implications for the transduction method used. As discussed in Section 2.4.1, piezoelectric devices are well suited to the application due to their high energy density and efficient mechanical-electrical transduction. However, not all piezoelectric materials are biocompatible [2], and so care must be taken in the design of a practical system to be situated inside the body. Compared to the interference possible with an electromagnetic or electrostatic system however, the piezoelectric system is much better suited to the application.

3 System modelling

An energy harvester that fits the requirements of the brief may be a complex system with numerous degrees of freedom and a large number of unknown variables (which might include unknown bending and coupling stiffnesses, material properties, and system damping). A model of a system would also neglect many of the complications of a practical system, whereby manufacturing tolerances, nonlinearities, and boundary conditions amongst others all present additional difficulties in prediction.

Therefore, a simplified model for simulation would allow many of the same conclusions in relation to translational and rotational systems to be drawn, without the added complexity of a full finite-element model. This section presents the simplifications made in the numerical model used, in addition to the rationale for the practical work carried out.

Manufacturing a prototype multi-degree-of-freedom system would be expensive, complex, and likely suffer reduced accuracy. Therefore, the practical prototype will utilise a single-degree-of-freedom system, with coupling to additional identical systems carried out numerically to determine the multi-degree-of-freedom system. Additionally, sourcing and manufacturing components at the scale required for an implantable biomedical device would be prohibitively expensive, and so the practical testing was carried out at a larger scale with scaling arguments used to rationalise the design for the specific use case.

3.1 Energy harvester architecture

As discussed in Section 2, a number of transduction methods are commonly used in energy harvesting devices. With the context of an implantable medical device (IMD) in mind, and having carried out research into other practical implementations, a piezoelectric system was selected for the experimental work. This is because such components are commercially available at a scale feasible for the project (taking into account ease of measurement using standard accelerometers, and ease of manufacture of a test rig to give translational and rotational inputs), and that their relatively high energy density and efficient mechanical-electrical transduction makes them well suited to the application.

Many piezoelectric modules are designed to harvest energy in bending, whereby the induced strain in the material results in a voltage output that can then be connected across a load to give a measurable power output. These are typically designed for a cantilever clamped arrangement, whereby the root of the module is clamped and the piezoelectric material can vibrate as a beam. Such an arrangement gives a simple model for the system, and its behaviour is well understood using Euler-Bernoulli beam theory, simplifying its simulation. For that reason, a cantilever clamped piezoelectric module was used for the experimental work.

3.2 Simplified cantilever model

$$\rho A \frac{\partial^2 x_2}{\partial t^2} + EI \frac{\partial^2 x_2}{\partial x_1^2} = f(x_1, t) \quad (9)$$

Carrying out a full characterisation of the cantilever clamped piezoelectric module would require use of the bending vibration PDE for an Euler-Bernoulli beam given in Equation 9.

However, a full model is far more complicated than necessary. As the suggested biomedical application requires a system with a low natural frequency, the cantilever requires a lower bending stiffness than that of a standard piezoelectric transducer. Therefore, a ‘stiffness reducing element’ of length d was included between the piezoelectric module and the root.

As the element has a far lower bending stiffness than the piezoelectric module, this governs this stiffness of the system, which can then be simplified to a single-degree-of-freedom with an effective mass, stiffness, and damping coefficient.

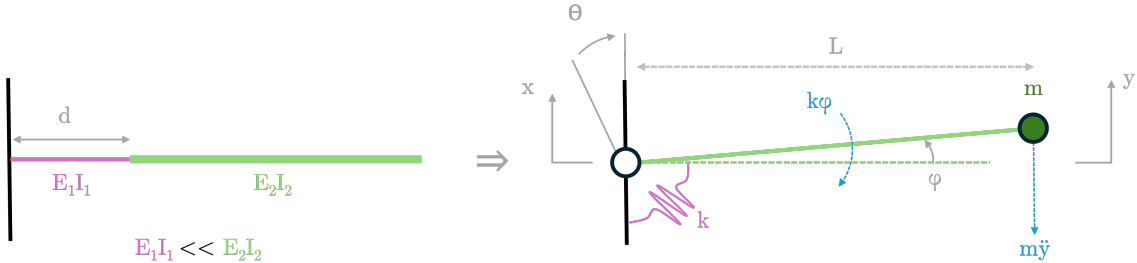


Figure 4: Diagram of the simplified cantilever model with translational and rotational input due to the stiffness reducing element.

Figure 4 illustrates the case in which the bending stiffness of the connecting element, $E_1 I_1$, is far smaller than that of the piezoelectric module, $E_2 I_2$. This results in a system model with a single output degree-of-freedom, the absolute tip displacement y , which results from a translational input x and a rotational input θ . The rotation of the beam ϕ is an intermediate variable given by:

$$\phi = \frac{y - x}{L} - \theta \quad (10)$$

The rotational stiffness due to the stiffness reducing element is k , resulting in a restoring torque $k\phi$. Combining this with the D'Alembert force at the tip and associating a damping with the relative velocity gives the equation of motion:

$$m\ddot{y} + c\dot{y} + ky = c(\dot{x} + L\dot{\theta}) + k(x + L\theta) = c\dot{z} + kz \quad (11)$$

Equation 11 can be solved numerically for a range of inputs and system parameters to simulate the behaviour of the harvester. For the practical rig, the tip acceleration of the cantilever can be measured using an accelerometer, and the output voltage of the piezoelectric module can be measured to determine the power output of the system. Rather than extensively modelling the relationship between the two (which will be a function of the material behaviour, clamping arrangement, amplitude, frequency

amongst other factors), an empirical model can be achieved by fitting parameters to the experimentally derived transfer function between the two.

3.3 Periodic structure model

A periodic structure is one which includes some degree of repetition in its composition, for example, alternating layers in a composite material. Such structures exhibit unique behaviour: in materials, this can lead to selective bandgap filtering of certain frequencies, for example in the foundations of a building, acting as a vibration isolator [12].

Periodic structures have a unique mechanical behaviour which is analogous to a *bandpass filter*. That is to say that their transfer function between input and output approaches a form whereby frequencies between ω_{low} and ω_{high} are ‘passed’ with a gain of k , whilst those outside of this range are attenuated. In a mechanical system, the lower frequency, ω_{low} , is governed by the mass and stiffness of the system, whilst the bandwidth, $b = \omega_{high} - \omega_{low}$, is controlled by the coupling stiffness between the degrees of freedom.

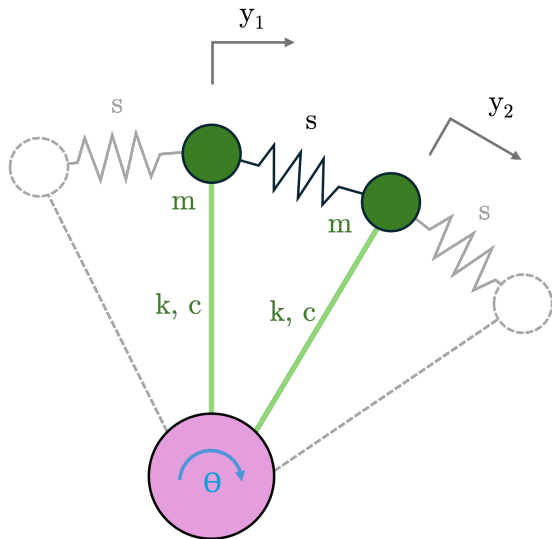


Figure 5: Schematic of a rotationally periodic system, with coupling stiffness s between each degree of freedom.

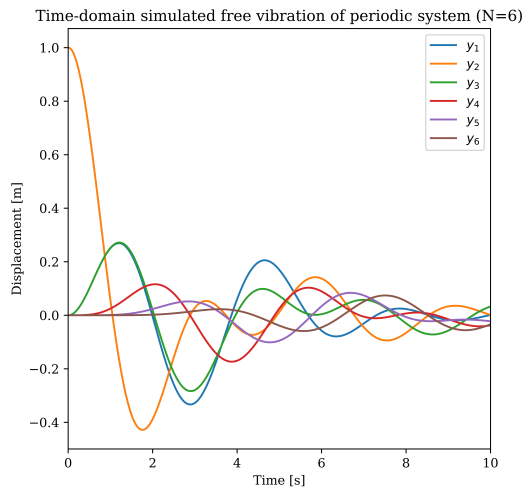


Figure 6: The simulated free vibration response of a 6 degree-of-freedom system with rotational periodicity.

Figure 5 shows an example of a N degree-of-freedom system with rotational periodicity, formed of light cantilevers with lateral stiffness k and lateral damping coefficient c with tip masses of m . The system can be subject to a rotational input at the base, and Figure 6 shows the simulated free vibration response of an example system where one member is initially displaced for the case when $N = 6$. More details on the numerical model used here can be found in Section 5.

$$\mathbf{M} = \begin{pmatrix} m & 0 & 0 & \dots & 0 \\ 0 & m & 0 & \dots & 0 \\ 0 & 0 & m & \dots & 0 \\ \vdots & \vdots & \vdots & \ddots & \vdots \\ 0 & 0 & 0 & \dots & m \end{pmatrix} \quad \mathbf{C} = \begin{pmatrix} c & 0 & 0 & \dots & 0 \\ 0 & c & 0 & \dots & 0 \\ 0 & 0 & c & \dots & 0 \\ \vdots & \vdots & \vdots & \ddots & \vdots \\ 0 & 0 & 0 & \dots & c \end{pmatrix} \quad (12)$$

The system can be described by the matrices in Equations 12 and 13. Notably, the mass and damping matrices are diagonal in this case, meaning that the system exhibits Rayleigh damping [13], whereby the damping matrix is proportional to the mass matrix, i.e. $\mathbf{C} = \frac{c}{m}\mathbf{M}$.

$$\mathbf{K} = \begin{pmatrix} k+2s & -s & 0 & \dots & -s \\ -s & k+2s & -s & \dots & 0 \\ 0 & -s & k+2s & \dots & 0 \\ \vdots & \vdots & \vdots & \ddots & \vdots \\ -s & 0 & 0 & \dots & k+2s \end{pmatrix} \quad (13)$$

Due to the coupling stiffnesses, the system's stiffness matrix is not diagonal, with the periodic form given by Equation 13.

$$\mathbf{A} = \begin{pmatrix} \mathbf{0} & \mathbf{I} \\ -\mathbf{M}^{-1}\mathbf{K} & -\mathbf{M}^{-1}\mathbf{C} \end{pmatrix} \quad (14)$$

The behaviour of the damped system in the frequency domain can be analysed using the state space transfer function matrix \mathbf{A} , given in Equation 14. The eigenvalues of the matrix \mathbf{A} give the natural frequencies of the system, and the eigenvectors are the mode shapes of the system. Solving for the eigenvalues of the matrix allows the calculation of the natural frequencies of the system to be calculated for any number of degrees of freedom N .

$$\omega_n = \begin{cases} \sqrt{\frac{k}{m}} & n = 1 \\ \sqrt{\frac{k+s}{m}} & n = 2, 3 \\ \sqrt{\frac{k+3s}{m}} & n = 4, 5 \\ \sqrt{\frac{k+4s}{m}} & n = 6 \end{cases} \quad (15)$$

Therefore, for the system with $N = 6$, the natural frequencies are given by Equation 15. Here, repeated natural frequencies are due to the system having degenerate or doublet modes because of its symmetry.

These analytic natural frequencies can be compared with the simulated transfer functions of the system to ascertain its bandpass effect. The system's transfer functions for a narrowband Gaussian input are shown for a system with $N = 6$ and $N = 30$ in Figure 7.

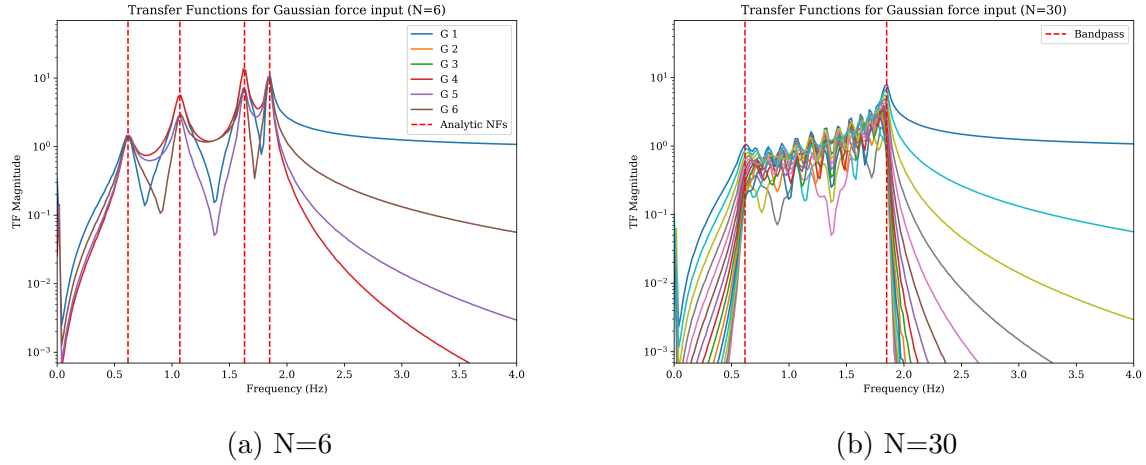


Figure 7: Simulated transfer functions for the two rotationally symmetric multi-degree-of-freedom systems showing the bandpass effect, with the same bandwidth but increased modal density.

From Figure 7, it can be seen that the system exhibits a bandpass effect; the bandwidth is determined by the coupling stiffness s , and the natural frequencies are determined by the mass and stiffness. As N becomes increasingly large, the system acts as a bandpass filter, and the design of an energy harvester can take advantage of this property.

If a harvesting system is to be used in an application where the input is known to be narrowband within a certain frequency range, the multi-degree-of-freedom system can be ‘tuned’ to this range by adjusting the coupling stiffnesses and natural frequency. This allows for the system to be designed to maximise the power output for a given input, where the single-degree-of-freedom equivalent would be limited by having a single resonant peak for energy harvesting.

In the context of IMDs, the heart beats within a relatively narrow range, most typically between 60 and 180 beats per minute, or 1 to 3 Hz. Therefore, a practical system could be designed to be ‘bandpass’ within this frequency range, and thus maximise the operating power output of the harvesting device. This could theoretically be tailored for a number of applications with differing frequency ranges, however the efficacy of this approach is subject to the practical limits on tuning the parameters of the system.

Experimental work will be carried out to determine the performance of a single-degree-of-freedom system, and the ‘bandpass theory’ results discussed here will motivate the scaling up of the device to a multi-degree-of-freedom system for practical use, avoiding the complexity of manufacturing and testing such a system directly.

3.4 Scaling for the use case

Construction of a device at the scale required for an IMD would be prohibitively expensive, and so the practical work focused on a centimetre scale device, coinciding with commercially available piezoelectric modules. In order to determine how the device would perform if the dimensions were reduced, a scaling argument was used. This states that the power output of the device scales linearly with its volume, which relates to Langley's bound for a system with constant density.

However, it remains an open question as to how the behaviour of the piezoelectric element scales. The model used assumes that the output voltage of the piezo module is proportional to its tip acceleration (when clamped in the simplified cantilever arrangement). Such a relationship may not in fact be linear with respect to the device dimensions, but a full electromechanical transduction model is beyond the scope of the project. Full exploration of the scaling argument would address the concerns with the model, and provide a more accurate prediction of the performance of the device at the scale required for an IMD.

4 Experimental work

4.1 Methodology

The experimental work described in this section aimed to determine whether an energy harvesting system might show an improvement in performance when subjected to a rotational input, rather than solely a translational input, in addition to providing an experimental benchmark for validating the numerical model of the system.

As discussed in Section 2.3, the translational performance of the device will be governed by Langley's bound, but additional rotational input may allow the system to circumvent this bound and provide a performance benefit for a given scale.

Therefore, an experimental rig was required that allowed for the performance of a cantilever clamped piezoelectric module to be tested under translational and rotational inputs, and inputs that are a combination of the two. This required that the input of the system be controlled, and the output of the system be measured, but also that the translational and rotational modes of the rig be decoupled to allow for measurement of the harvester's performance independently of the rig.

The experimental work first entailed the design, iteration, and characterisation of the rig to meet the requirements of the brief. Then the rig was used to determine the performance of the system for the inputs described, and the behaviour of the system was used to inform the numerical model for comparison with the experimental results.

Two experiments were carried out for each of the three input cases: the first to determine the performance and linearity of the system under a range of input amplitudes, and the second to ascertain the power output of the system for a range of resistive loads through the optimal value for power matching.

4.2 Test rig design

In order to measure the response of the piezoelectric module to both translational and rotational inputs, a test rig was required that could provide both types whilst minimising damping so that the true response of the system could be measured. Using a bearing to facilitate the rotation of the system would introduce too much damping, especially for small angles of rotation, and so a base supported on wires was used. This allows for the base of the rig to move in the x and y directions by the shear bending of the wires, and for the whole system to rotate about the z-axis when the supports undergo torsion. The rig then applies this input to the single-degree-of-freedom harvester, which is a clamped piezoelectric cantilever.

This section presents the initial differential input concept of the rig, and the design iteration to improve the decoupling between the translational and rotational modes that resulted in the final input arrangement used.

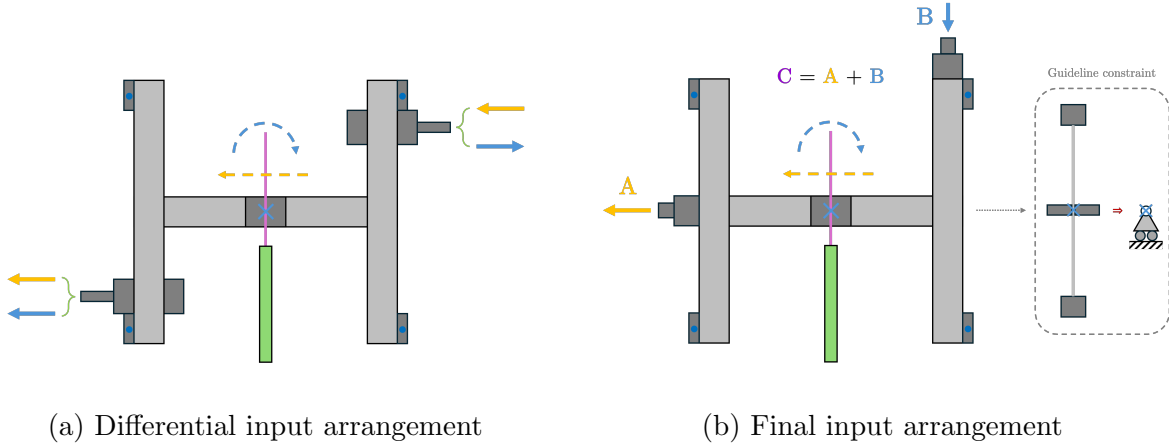


Figure 8: Comparison in plan view of the initial differential input arrangement (a) and the final arrangement (b) annotated with the input types. Orange represents translational input, and blue represents rotational input to the base of the green piezo cantilever.

Figure 8A shows the initial differential input arrangement, alongside the final input arrangement used for the experimental work in Figure 8B. The initial arrangement utilised a pair of opposing shakers mounted off-centre to the horizontal centreline of the base. When the two shakers were driven in phase, the base would undergo a rotational input about the centre of the rig, providing a rotational input to the base of the cantilever. When driven out of phase, the base would undergo a translational input in the x-direction, providing a translational input to the base of the cantilever. The attachment of the shakers to the base was by an adjustable clamp to ensure alignment of the shakers, and through flexures to ensure that any off-axis forces provided by the shakers were reduced.

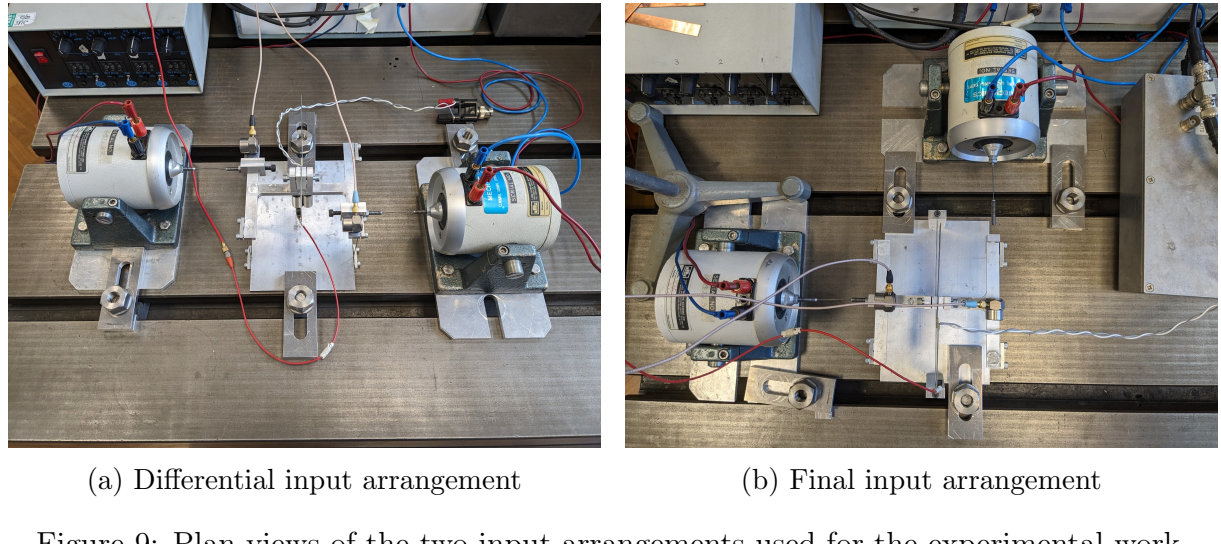


Figure 9: Plan views of the two input arrangements used for the experimental work.

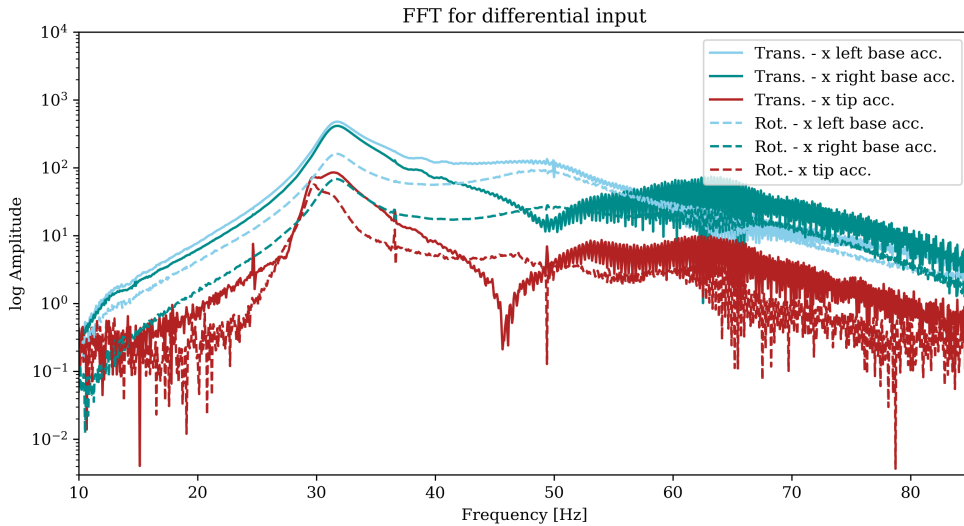


Figure 10: Plot of the accelerometer measurements in the frequency domain for the translational and rotational inputs to the differential rig in Figure 9A.

Figure 9A shows the practical differential input arrangement, complete with two accelerometers attached to the base and one at the tip of the cantilever, all in the x direction. The shakers were driven by a two channel amplifier with an identical 10 to 110 Hz sweep signal from the PC as the input. The amplifier utilised a variable phase switch to allow for the shakers to be driven in phase or out of phase for the rotation and translation cases respectively.

Figure 10 shows the resulting output of the system in the frequency domain for each of the accelerometers for the translation input (solid line) and rotational input (dashed line). For the translation and rotation modes to be decoupled, the rotational input should not cause significant excitation of the translation mode, and vice versa. However, analysis in the frequency domain shows that this is not the case, and that the ‘rotational’ input causes significant translation. Additionally, the amplitude of the rotation on the left and right of the rig was not equal, indicating that the system was not rotating about the centre as expected. Therefore, the design of the rig was iterated to improve this decoupling.

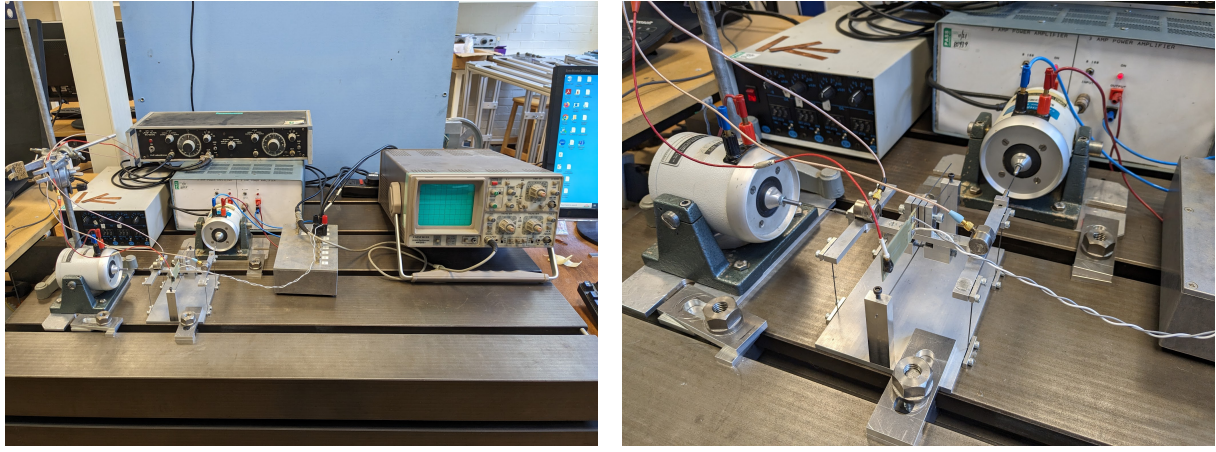
Figure 9B shows the final input arrangement with the translation shaker mounted along the centreline in the x direction, and the rotation shaker mounted off-centre in the y direction. The same amplifier was used, but the mode of input adjusted by the connection of the shakers to the base (individually or simultaneously for the three input combinations).

Also shown in Figures 8B and 9B is the addition of a guideline to the base, fitted to improve the decoupling between the translational and rotational modes of the rig. The structure clamps onto a steel guideline which restricts translation in the y direction, whilst still allowing translation in the x direction and rotation about the centre of the rig as the wire is more easily deformed transversely than longitudinally.

The length of the cantilever, shown in Figure 4 as length d , can be adjusted using the clamping arrangement on the rig. Setting this length sets the natural frequency of the fundamental mode of the cantilever, and so is important when it comes to the performance of the system. Having characterised the base modes of the rig, the cantilever was clamped

to give a fundamental frequency that was sufficiently separated from these modes so that the cantilever mode was distinct. This was achieved by trial and error and discussed in Section 4.4.

4.3 Equipment



(a) Overview of the setup

(b) Semi-isometric view of the rig

Figure 11: Overview of the experimental lab set up, including the test rig and associated components (a), and a semi-isometric view of the rig, showing the sensor locations and clamping arrangement (b).

Figures 11A and 11B show the experimental setup in the South Wing Vibration Lab used for the practical work. The rig was mounted on a large steel table to reduce the effect of external vibrations on the system, with slots for clamping. A PC running *pydvm* [14] was used for data acquisition and input generation, managed through a National Instruments USB DAC. The output was connected to a power amplifier via a low pass filter to remove digital artefacts, before being connected to the two shakers. The accelerometers used are discussed in Section 4.3.2, and were connected to a charge amplifier to convert the output to a voltage signal, before being connected to the DAC for data acquisition. The piezoelectric module was also connected to the DAC via a soldered connection for data acquisition of the output voltage. An analogue oscilloscope was used to visualise the output during testing.

4.3.1 Piezoelectric component

The piezoelectric component used was a S233-H5FR-1107XB piezoelectric bending transducer [15] manufactured by Mide, which is a sealed unit with two active layers. The material is PZT 5H, with FR4 shim material, with an area of 1.1 by 0.7 inches (or 27.8 by 18.0 mm). The design operation is in bending in the x direction.

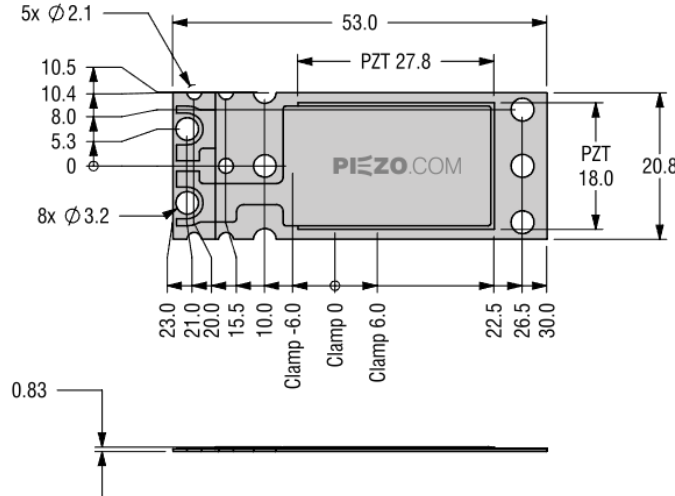


Figure 12: Technical drawing of the piezoelectric bending transducer used in the experimental work in plan and elevation, supplied by the manufacturer [15] with dimensions in mm.

4.3.2 Instrumentation and data acquisition

To apply the three input types outlined in Section 4.2, the mechanical connections of the rig to the shakers were adjusted. For Type A or translational input, a single shaker was connected along the rig's centreline in the x direction. For Type B or rotational input, a single shaker was connected off-centre in the y direction. For Type C or combined input, both of these shakers were connected to the rig simultaneously.

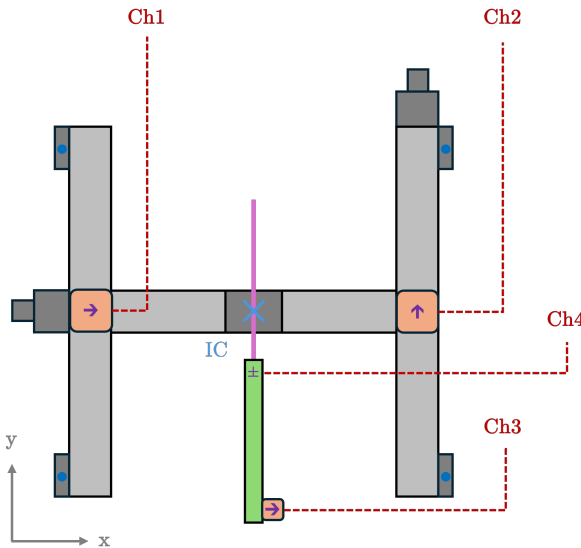


Figure 13: Representative diagram of the rig in plan annotated with the instrumentation used for the experimental work.

Table 2: Descriptions of the instrumentation per channel used for the experimental work.

Channel no.	Instrumentation	Description
0	pydvma	Digital output
1	DJB A/21 accelerometer	Base translation in the x-direction
2	DJB A/21 accelerometer	Base translation in the y-direction
3	Endevco 2222c	Cantilever tip translation in the x-direction
4	S233 piezoelectric bending transducer	Piezoelectric voltage due to motion

Figure 13 shows the rig in plan view with the instrumentation and logging channel used for the experimental work, and Table 2 details the equipment used for each channel.

The signal used to drive the shakers was provided by the PC, using *pydvma* [14] to supply a 10 to 85 Hz linear frequency sweep. This range was found to be the most suitable for the modes of the system following calibration experiments. This digital output was passed to the NI USB-6212 DAC operating at ± 5 V, before the analogue output was passed through a low pass filter to remove any digital artefacts. This output was then split and fed into the two input channels of the dual power amplifier, which supplied the input to the two shakers. The digital output signal was logged as Channel 0 in *pydvma* for reference.

Three accelerometers were used to measure the response of the system: two larger DJB A/21 accelerometers were used to measure the base translation in the x and y directions, and a smaller Endevco 2222c accelerometer was used to measure the tip translation in the x direction. These accelerometers were calibrated by attaching them together along their measurement axes and driving them with a known shaker. The output of the accelerometers were then set to be equal using the gain settings on the charge amplifier. The calibrated accelerometer signals were then passed to the DAC and logged as Channels 1, 2, and 3 in *pydvma*.

The locations of the accelerometers were chosen to characterise the translational and rotational modes of the rig. Channel 1 measured the effective translational input of the rig, whilst Channel 2 measured the effective rotational input. These could then be compared with Channel 3 to show the transfer function of the cantilever with respect to the base motion, achieving the aim of the experimental work in neglecting the modes of the rig.

Additionally, the output voltage of the piezoelectric module was measured using the DAC and logged as Channel 4 in *pydvma*. This was achieved via a soldered connection to a bayonet connector, which also allowed load resistances to be connected in parallel as discussed in Section 4.7. The output of the piezoelectric module was also checked using an analogue oscilloscope to verify its output voltage.

4.4 Translational, rotational, and combined inputs

The modes of rig were determined by taking the Fast Fourier Transform (FFT - implemented in *pydvma*) of the accelerometer and voltage time data for each of the three input types. This aided identification of the system's modes in the frequency domain, and allowed them to be characterised as either due to the behaviour of the rig, or the behaviour of the cantilever.

The practical experiment was intended to determine the performance of a single-degree-

of-freedom harvester subject to translational and rotational input, and so any behaviour due to the specific rig must be isolated. In order to validate this single-degree-of-freedom cantilever behaviour, this mode must be well separated from those due to the rig. Analysis in the frequency domain allowed for the natural frequency of the cantilever to be adjusted (using clamping distance d) so that the ‘operating region’ of the system was well separated with minimal modal overlap from the modes of the rig.

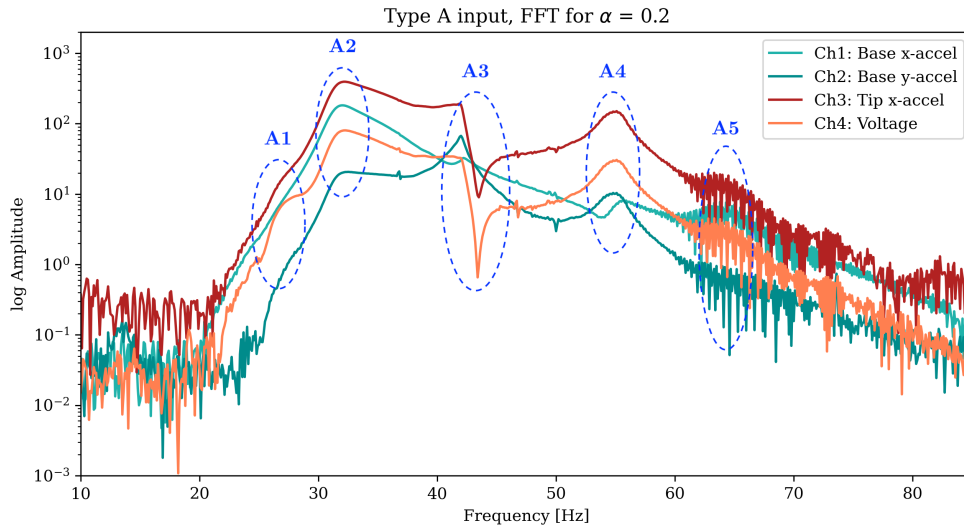


Figure 14: The Fourier transform of each measured channel in the input frequency range for the case of a Type A translational input. Annotations indicate the modes seen.

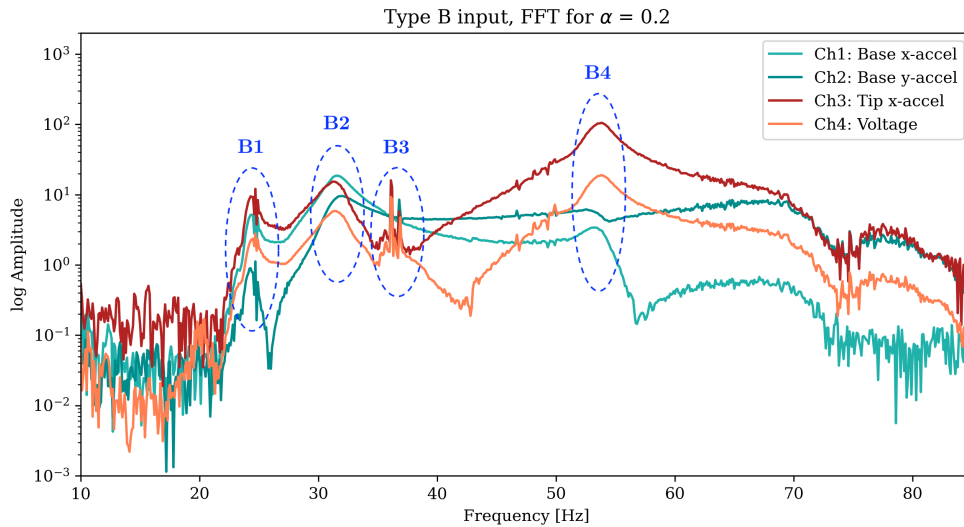


Figure 15: The Fourier transform of each measured channel in the input frequency range for the case of a Type B rotational input. Annotations indicate the modes seen.

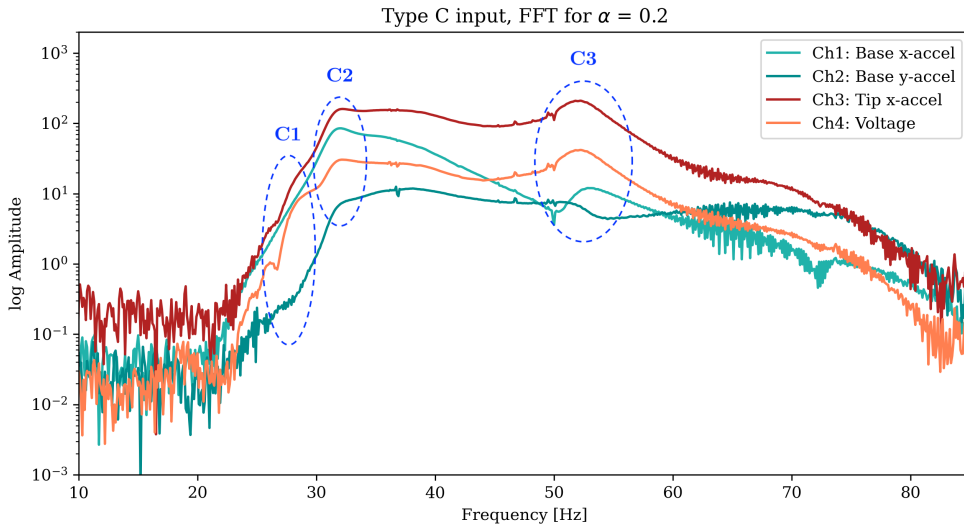


Figure 16: The Fourier transform of each measured channel in the input frequency range for the case of a Type C combination input. Annotations indicate the modes seen.

Table 3: Frequencies and brief descriptions of the modes and features annotated in the FFTs for each of the three input types (Figures 14, 15, and 16).

Label	Frequency [Hz]	Description
A1	26	Low amplitude peak, likely associated with rotation mode of the rig.
A2	32	High amplitude peak due to the translation mode of the rig.
A3	42	Marked dip in the cantilever motion, likely due to instantaneous centre.
A4	54	Fundamental cantilever mode, set using the clamped length d .
A5	64	Second harmonic of mode A2, verified experimentally.
B1	25	Rotation mode of the rig in all channels, also seen in A1.
B2	32	Translation mode of the rig, also seen in A2.
B3	37	Rig motion resulting in non-modal behaviour of the cantilever.
B4	54	Fundamental cantilever mode, as seen in A4.
C1	27	Rotation mode of the rig, less pronounced than A1 and B1.
C2	32	Translation mode of the rig, less pronounced than A2 and B2.
C3	52	Cantilever mode, now wider bandwidth and lower frequency than A4 and B4.

Figures 14, 15, and 16 show the FFT of the time data for each of the channels for input types A, B, and C respectively. The identified modes of the system are then labelled and described in Table 3.

Type A input shows five modes within the frequency range of the input sweep. Two of these, A1 and A2, at 26 and 32 Hz correspond to the motions of the rig, governed by its mass and the stiffness of its supports. ‘Mode’ A3 is more of a feature, and is likely due to the superposition of the rig’s translational and rotational modes. As the frequency increases, the balance of these two motions evolves, and the dip at 42 Hz likely shows that the instantaneous centre of this motion aligns with the base of the cantilever. This results in this frequency acting as if a node for the cantilever, whilst the base is still in motion.

Mode A4 is the fundamental cantilever mode of the rig, set by trial and error to be well separated from the base motion, and the well defined peak appears to have low modal

overlap, suggesting that the system can be considered with a single-degree-of-freedom within this operating range. The final mode, A5, is only visible as a slight rise. However, this was experimentally verified to be the second harmonic of mode A2, where 64 Hz is the second harmonic of the 32 Hz translation mode of the rig. This was achieved by driving the system between 30 and 35 Hz, and observing that the system had a 64 Hz response in the frequency domain. This is an example of nonlinear behaviour, and the nonlinearity of the system is further explored in Section 4.6.

Type B input shows four modes within the frequency range of the input sweep, with modes B1 and B2 mirroring those seen in A1 and A2. Mode B3 appears to be a feature of the system rather than a mode, whereby the cantilever element exhibits some motion, likely due to the same underlying behaviour as mode A3. Mode B4 is again the fundamental cantilever mode, once again showing good separation from the base modes.

The FFT from the Type C input is far more level than the other two, but still shows three modes: the two rig base modes as before, and the fundamental cantilever mode. C3 is a broader peak with a slightly lower natural frequency than modes A3 and B3, but is still due to the same cantilever motion. This might suggest that the single-degree-of-freedom model is less valid for this input type, but within the operating range, the system is still well separated from the base modes (seen by the flatter spectra for the base accelerometers).

4.5 System characterisation

Having characterised the system in the frequency domain for each of the three input types, the transfer functions of the system were calculated. The entirety of the 4×4 transfer function matrix was calculated for each of the three input types, but for harvesting behaviour and performance, four were of interest:

- G_{13} : the transfer function between the base x-acceleration and the cantilever tip x-acceleration, used to determine the relationship between the base motion in translation and the cantilever motion.
- G_{14} : the transfer function between the base x-acceleration and the piezoelectric voltage output, used to determine the relationship between the base motion in translation and the harvester output voltage, then power.
- G_{23} : the transfer function between the base y-acceleration and the cantilever tip x-acceleration, used to determine the relationship between the base motion in rotation and the cantilever motion.
- G_{24} : the transfer function between the base y-acceleration and the piezoelectric voltage output, used to determine the relationship between the base motion in rotation and the harvester output voltage, then power.

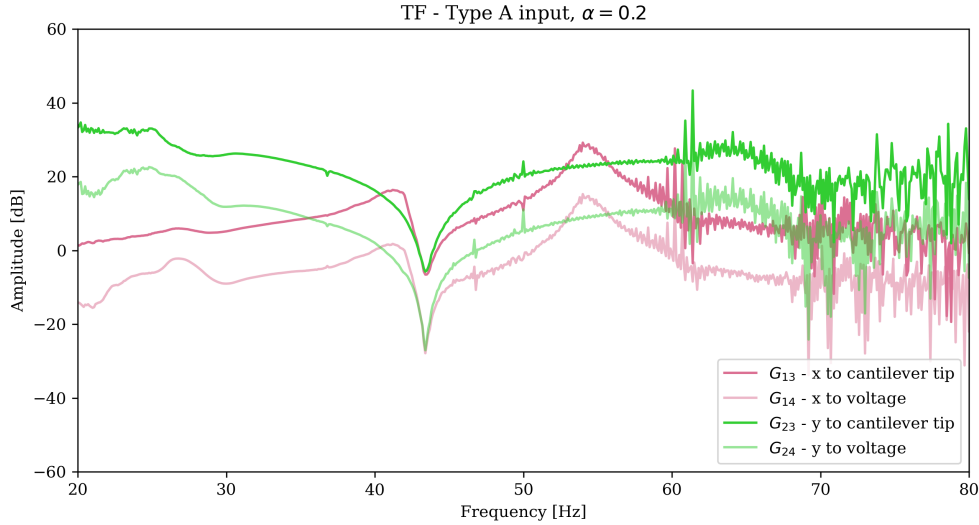


Figure 17: The aforementioned experimental transfer functions of the system for the Type A translational input.

Figure 17 shows G_{13} , G_{14} , G_{23} , and G_{24} for the Type A translational input between 20 and 80 Hz. From pairs G_{13} & G_{14} and G_{23} & G_{24} , it can be seen that the relationship between the cantilever tip x-acceleration and the piezoelectric voltage output is approximately linear. This is seen as $G_{14} = G_{13} \cdot G_{34}$, and then pairs appear to only differ by a constant factor in amplitude, β , i.e. $G_{34} \approx \beta$.

At around 43 Hz, both the x and y behaviours of the system are coupled, and exhibit a dip in amplitude. This is likely due to the same instantaneous centre alignment discussed in Section 4.4. For the translational behaviour, the transfer function shows the cantilever mode at 54 Hz, whilst the y transfer function is relatively flat. This suggests that the system's operating range, where it acts as if a single-degree-of-freedom system subject to translational base excitation, is between 45 and 65 Hz for Type A input.

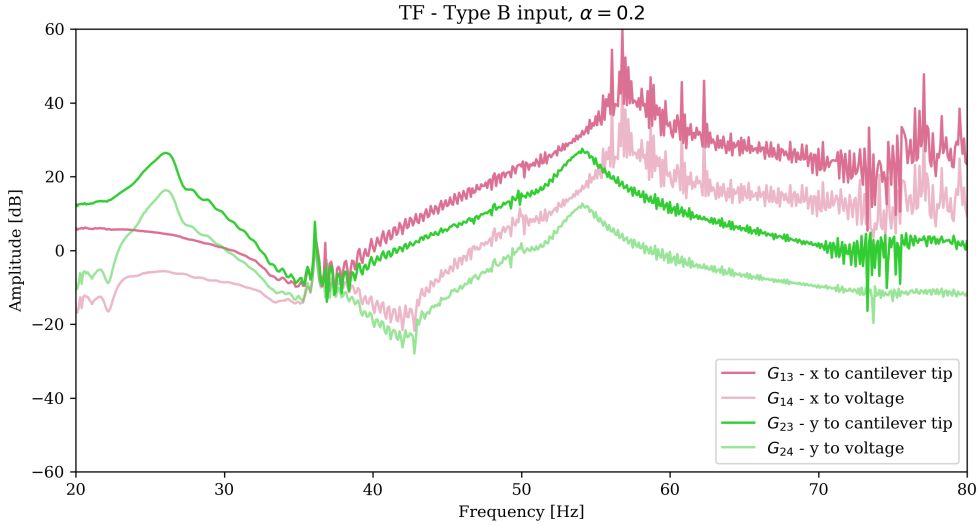


Figure 18: The aforementioned experimental transfer functions of the system for the Type B rotational input.

Figure 18 shows the same transfer functions as Figure 17 but for the Type B rotational input instead. The same linear relationship between the cantilever tip x-acceleration and the piezoelectric voltage output can be seen, but the overall behaviour is more complex, particularly at lower frequencies. Neglecting the behaviour below 40 Hz as motion due to the rig modes, the operating modes and range of the system can be assessed.

The same 54 Hz translational cantilever mode is still present in the y transfer functions, but the x transfer function appears to show a similar mode at a slightly higher frequency, approximately 58 Hz. This would suggest that the system has two cantilever modes in the operating mode, and so the operating bandwidth for Type B is slightly wider, albeit between the same frequencies of 45 and 65 Hz.

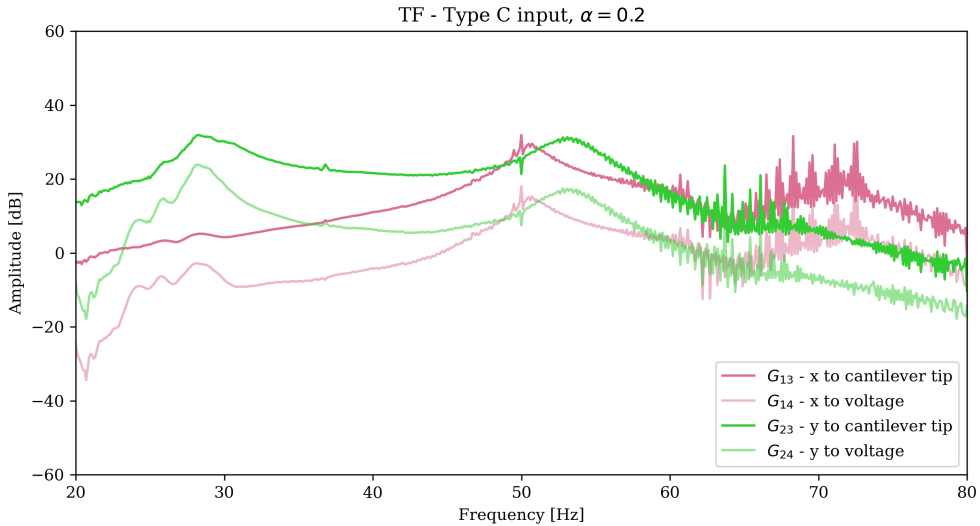


Figure 19: The aforementioned experimental transfer functions of the system for the Type C combination input.

Figure 19 shows the same transfer functions as Figure 17 but for the Type C combination input instead. Once again, the linear cantilever-voltage relationship is evident, and fewer modes can be seen compared with the Type A and B systems. Two cantilever modes can be seen, again at 54 Hz, but also at a lower 50 Hz in the x transfer functions. This gives the Type C system a wider operating bandwidth with the two modes, but once again the system appears to operate best between 45 and 65 Hz.

From analysis of the transfer functions of the system for each of the prescribed input types, the system's operating range is determined to be between 45 and 65 Hz. This is the range in which the system behaves as if it is a single-degree-of-freedom system subject to base excitation comprised of translation and/or rotation. Within this range, the system's behaviour can be replicated with the numerical model, and represents the harvesting range of the device.

Additionally, the transfer functions show the relationship between the tip x-acceleration and the piezoelectric voltage output, G_{34} to be approximately linear within the operating range, which will be utilised in Section 6.1 when using the experimental data to inform the numerical model.

4.6 Amplitude experiments

In order to ascertain the linearity of the system, a range of input amplitudes were used for each of the three input types (translation ‘Type A’, rotation ‘Type B’, and combined ‘Type C’) and the resulting behaviour of the system measured.

$$z(t) = \alpha \cos(\omega(t)t) \quad (16)$$

Equation 16 describes the form of the input used, where $z(t)$ is the input in arbitrary units for each of the three cases, $\omega(t)$ denotes the linear frequency sweep between 10 and 85 Hz, and α is the amplitude of the input. The standard amplitude used in the other experiments was $\alpha = 0.2$ at which the system appeared to behave linearly (without clipping of input, rattle, or any other undesirable effects).

Therefore α was varied between 0.05 and 0.5 for each of the input types. α represents the input parameter in *pydvma*, and as the hardware was operating between ± 5 V, the input signal to the shakers was between 0.25 and 2.5 V. The accelerometer and piezoelectric output voltages were measured to determine the transfer function of the system as a function of the input amplitude for each of Type A, B, and C inputs.

Table 4: Table of the input amplitude α used for each of the amplitude experiments for each of the three input types.

Set	0	1	2	3	4	5	6	7
α	0.05	0.10	0.15	0.20	0.25	0.30	0.40	0.50

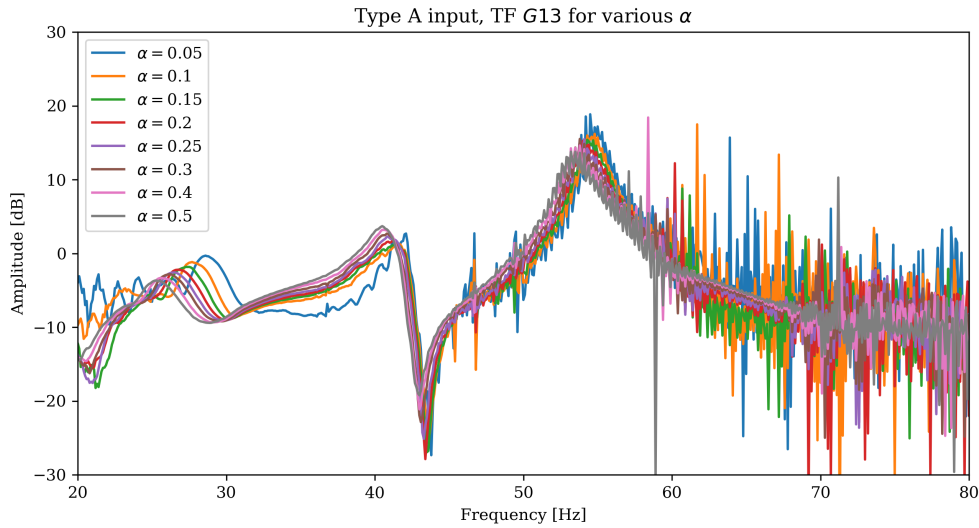


Figure 20: The experimental transfer function (G_{13}) of the system for a range of input amplitudes α when driven by the Type A translational input.

Figure 20 shows the transfer function between the base x-acceleration and the cantilever tip x-acceleration between 20 and 80 Hz. This transfer function highlights the behaviour of the harvester cantilever for a given input of the base, attempting to isolate any behaviour due to the rig and shakers interacting. The transfer function is shown for a range of input amplitudes α for the Type A translational input.

From the plot, it can be seen that the transfer function is broadly similar in amplitude and shape across all values of α . In the lower frequency range, between 25 and 40 Hz where the behaviour is coupled to the rig, the transfer functions show some variation in amplitude, and a larger variation in the natural frequency of the peaks. This highlights *softening* behaviour, whereby the effective stiffness and therefore natural frequencies of the system decrease with increasing amplitude of the input.

In the harvester's working region, between 45 and 65 Hz, the same softening behaviour can be seen, but the changes in amplitude and frequency are far less significant. The cantilever peak at 54 Hz ‘bends’ to the left of the plot for increasing input amplitude, but considering that this is small, the strength of the system’s nonlinearity would appear to be weak within the amplitude and frequency ranges tested.

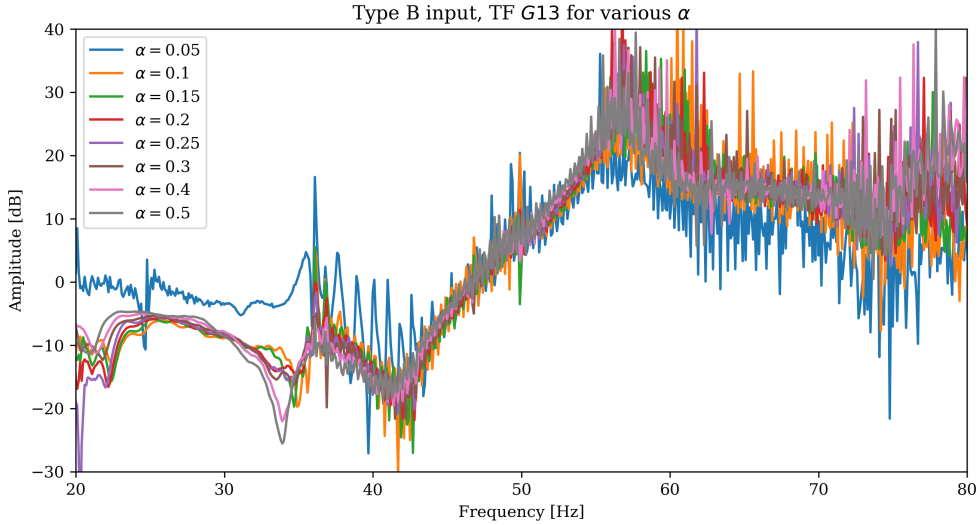


Figure 21: The experimental transfer function (G_{13}) of the system for a range of input amplitudes α when driven by the Type B rotational input.

Figure 21 shows the same transfer function as Figure 20 but for Type B rotational input instead. Here, the rig behaviour below 40 Hz is less clear and the overall noise level is higher. For the case of $\alpha = 0.05$, there is significant deviation in behaviour, and this may be due to the input being insufficiently large to fully excite rotational motion, leading to a low signal-to-noise ratio. However, the same weak softening nonlinearity can be seen in the position of the 54 Hz cantilever peak.

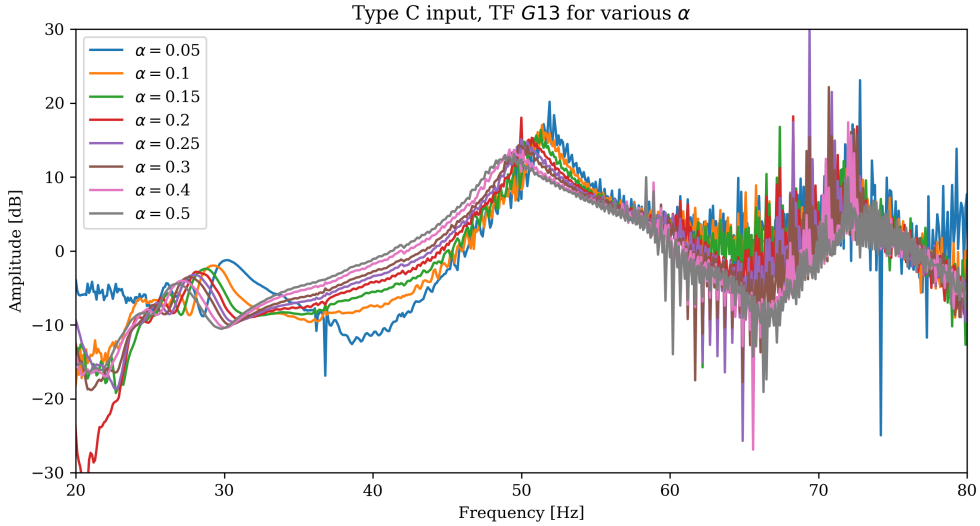


Figure 22: The experimental transfer function (G_{13}) of the system for a range of input amplitudes α when driven by the Type C combination input.

Figure 22 shows the same transfer function as Figure 20 but instead for Type C combination input. The same softening nonlinear behaviour can be seen, but this is more severe, particularly in the frequency reduction of the cantilever peak. The distinction

between rig and cantilever behaviour is less clear, but it can be seen that softening occurs across the whole range.

From Figures 20, 21, and 22, it can be seen that the system exhibits weak softening nonlinear behaviour for each of the three input arrangements. This is most pronounced for the Type C combination input, but generally the effect of the nonlinearity is weak across the operating frequency range.

The joints present on the rig are the most likely source of the nonlinear behaviour; these are in the form of threaded connections to the shakers, clamping of the guideline and supports, and the clamping of the piezoelectric module. For larger input amplitudes, the joints experience more microslip at their respective interfaces, and so appear less stiff as the amplitude increases. This results in the reducing natural frequencies observed in the practical transfer functions.

Having determined that the nonlinearity exhibited is relatively weak, the system can be considered to be linear for the purposes of the numerical model. This reduces the complexity, and allows use of the frequency domain model as well as the time domain model for the system, giving two routes of validation for the practical results.

4.7 Harvesting experiments

In order to determine the harvesting performance of the system for each of the three input types, a power matching experiment was carried out. The value of the load resistance was varied for the same input sweep between 10 and 85 Hz with $\alpha = 0.2$, and the accelerations and voltage output of the piezo module were measured to determine the power output of the system for each resistance.

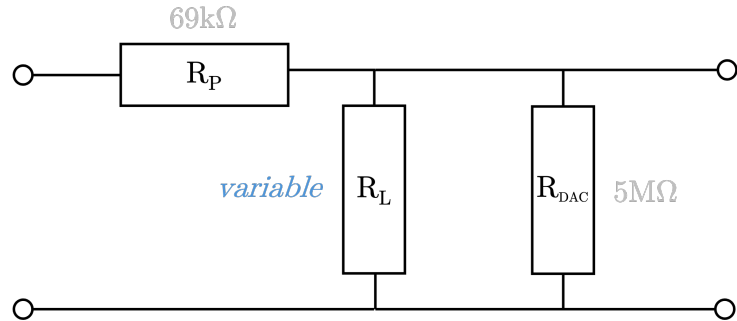


Figure 23: Annotated circuit diagram for the experimental harvesting setup.

$$P_{RMS} = \frac{V_{RMS}^2}{R_L} = \frac{\left(\frac{V_{PP}}{2\sqrt{2}}\right)^2}{R_L} \quad (17)$$

Figure 23 shows the circuit arrangement used for measuring the harvesting performance of the system. The resistance of the piezoelectric module is given by $R_P \approx 69 \text{ k}\Omega$, and load resistor R_L is connected across the large impedance of the DAC, $R_{DAC} = 5 \text{ M}\Omega$. The value of the load resistor was varied to determine the optimal power output of the system, and the output voltage of the piezo module was measured. From this, the RMS power output of the system at the optimal frequency can be calculated using Equation 17.

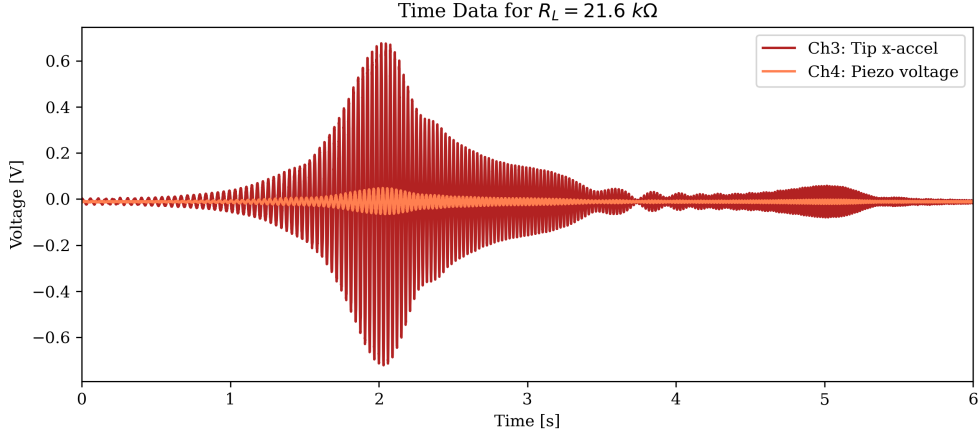


Figure 24: Example of the experimental tip acceleration voltage and piezoelectric output voltage against time for Type A input with $R_L = 21.6 \text{ k}\Omega$.

Table 5: Table of the load resistor values used for each of the power matching experiments for each of the three input types.

Set	0	1	2	3	4	5	6	7	8	9	10
R_L [$\text{k}\Omega$]	2.2	4.4	6.8	13.6	21.8	43.6	68	100	216	466	669

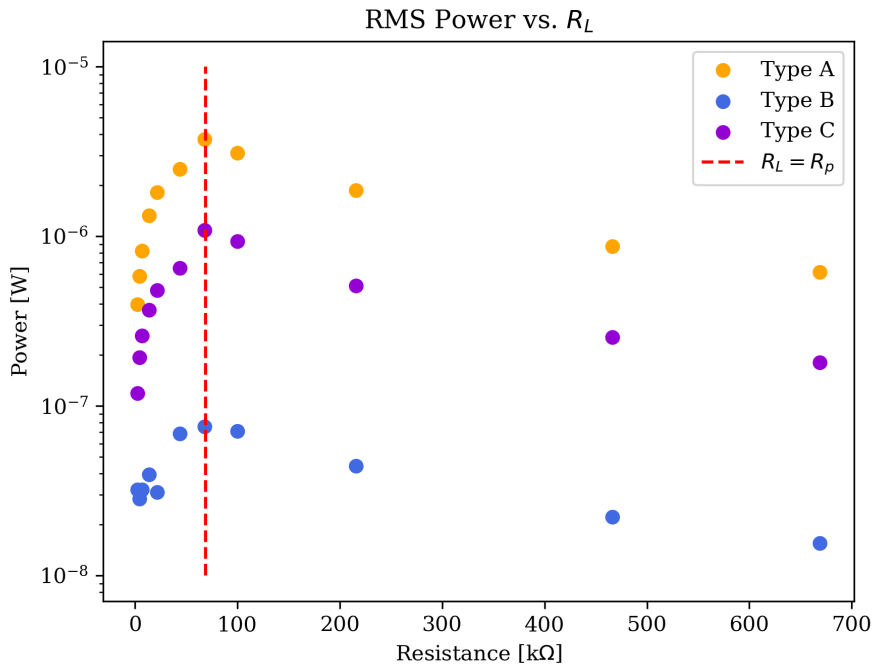


Figure 25: The peak power output of the system as a function of the resistance of the load resistor for each of the input types.

Figure 25 presents the peak RMS power output of the system for each R_L value for each of the input types. The results show that the system exhibits a peak power output when

$R_L = R_P$ for each of the input types, as expected for optimal power matching, with the power lower than this peak for resistances above and below this value.

The power output of the system is highest for the Type A translational input, peaking at approximately $4 \mu\text{W}$, with the rotational Type B input providing far less power. The rationale of the project would suggest that combining both input types would provide better performance, but the experimental results show that the Type C input performs significantly worse than the purely translational input.

However, these results are in terms of the peak RMS power of the specific rig in response to the input, which is nominally the same across the three input types. Practically, the different input types are controlled by connecting the shakers alternately or together. So for Type A and B, one shaker is connected, and Type C both are connected. The connection of the shakers has a significant effect on the amplitude of the mechanical input to the system, and so Type B and C resulted in a far lower acceleration amplitude of the base and cantilever. Therefore, scaling the power results for each of the respective input types by the resulting base acceleration should provide a more comparable measure of the harvesting performances.

$$P'_{RMS} = \frac{P_{RMS}}{a_{RMS}^2} \leq M_T \quad (18)$$

Equation 18 describes the scaling of the power output of the system by the respective input acceleration *squared* for each of the input types. For Type A, the base x-accelerometer (*Ch 1*) was used, for Type B, the base y-accelerometer (*Ch 2*), and for Type C, the magnitude of the two was used given that they are orthogonal.

Scaling by the input acceleration squared in units of g^2 was chosen as it best relates to Langley's bound in Equation 1, where S_0 is the input acceleration spectral density in units of $(\text{ms}^{-2})^2 \cdot \text{Hz}^{-1}$. This scaling allows for the comparison of the power output of the system for each of the input types with the bound, as P' is now less than or equal to the effective mass of the harvester M_T .

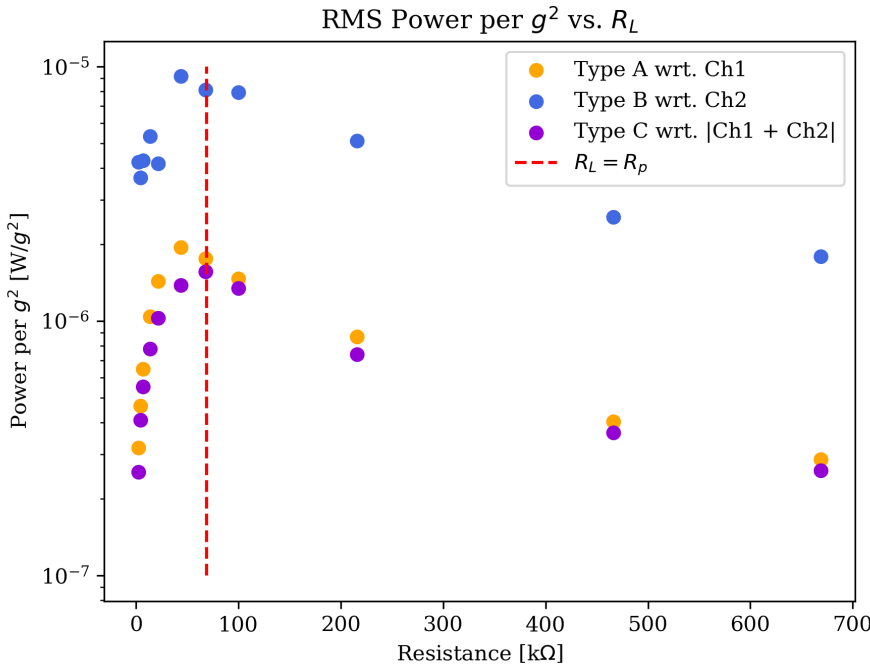


Figure 26: The peak RMS power output of the system as a function of the load resistance for each of the input types, scaled by the respective RMS input acceleration squared.

Figure 26 shows the peak RMS power output of the system for each R_L value for each of the input types, scaled by the respective input acceleration squared. The scaled experimental results suggest that the rotational Type B input performs significantly better than the translational Type A input for a given input amplitude. However, the Type C input still performs worse than the two individual inputs it is nominally comprised of.

This result appears to contradict the expected findings of the project, but further analysis of the Type C input behaviour raises a number of points. Firstly, the Type C input is a combination of input from the two shakers, both of which have the same input signal from the output of the PC followed by the low-pass filter. As the input used is a harmonic sweep, the two shakers should be in phase at all times. This raises the question of whether the phase has an effect on the harvesting performance of the system. Secondly, the Type C input uses two nominally identical shakers, but in reality, the two were found to respond with different amplitudes to the same input signal. Whilst the Type C formulation was intended to be a representative combination input, the misbalance of the shakers may have inadvertently reduced performance.

Therefore a suggestion for future work would be an experiment using balanced shakers with a variable phase shift between them to ascertain the effect of the composition of a combined input on the harvesting performance of the system. Another alternative would be the use of separate, uncorrelated narrowband white noise inputs whereby the phase is not a parameter like it is with harmonic inputs. However, this would require a more complex experimental setup.

Present experiments have shown that the separate translational and rotational inputs are effective for harvesting, but more careful control of their combination would hopefully be able to characterise the parameters conducive to optimal performance.

5 Simulation work

In order to scale the results of the single-degree-of-freedom experimental system to a multi-degree-of-freedom system as described in Section 3, a numerical model was required. To that end, two approaches were taken: firstly for linear systems, the behaviour can be calculated in the frequency domain alone. Secondly, for nonlinear systems, the behaviour must be calculated in the time domain, so a Newmark-Beta scheme was implemented in Python. Both the time and frequency domain models can be used in conjunction with the experimentally determined parameters of the system to predict the performance of a multi-degree-of-freedom system and inform the design of a device for a specific purpose, like that for an implantable medical device (IMD).

5.1 Single-degree-of-freedom systems

Having defined the parameters of the system and the time step and duration of the simulation, an implementation of the Newmark-Beta scheme [16] was used to solve the governing equations of motion.

$$\dot{y}_{n+1} = \dot{y}_n + (1 - \gamma)\Delta t \ddot{y}_n + \gamma\Delta t \ddot{y}_{n+1} \quad (19)$$

Equation 19 is the Newmark-Beta routine, in this case, implemented in Python, where γ is a parameter associated with the scheme. This results in an output vector y from a combined base input $z = x + L\theta$, as described in Equation 11.

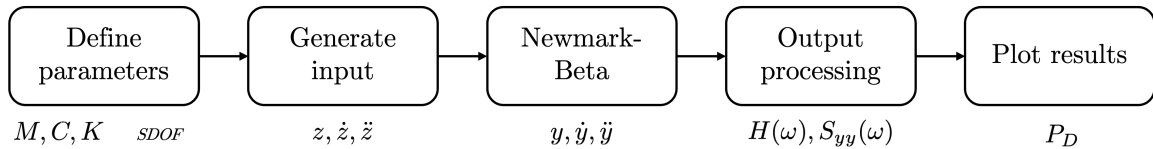


Figure 27: Flowchart of the time-domain simulation process for a single-degree-of-freedom system, where $z = x + L\theta$.

Figure 27 illustrates the simulation process used for the time-domain simulation of the system. The system parameters are defined, and an input is generated, which in this case is a bandlimited Gaussian white noise signal, practically realised with a fifth-order bandpass Butterworth filter in the specified frequency range. Both are then input to the Newmark-Beta function, resulting in the output displacement, velocity, and acceleration of the system. These are then processed to determine the frequency behaviour of the simulated system, and the power output of the system over time, using Rayleigh's form, $P_D = c(\dot{y} - \dot{z})^2$, for a single-degree-of-freedom system.

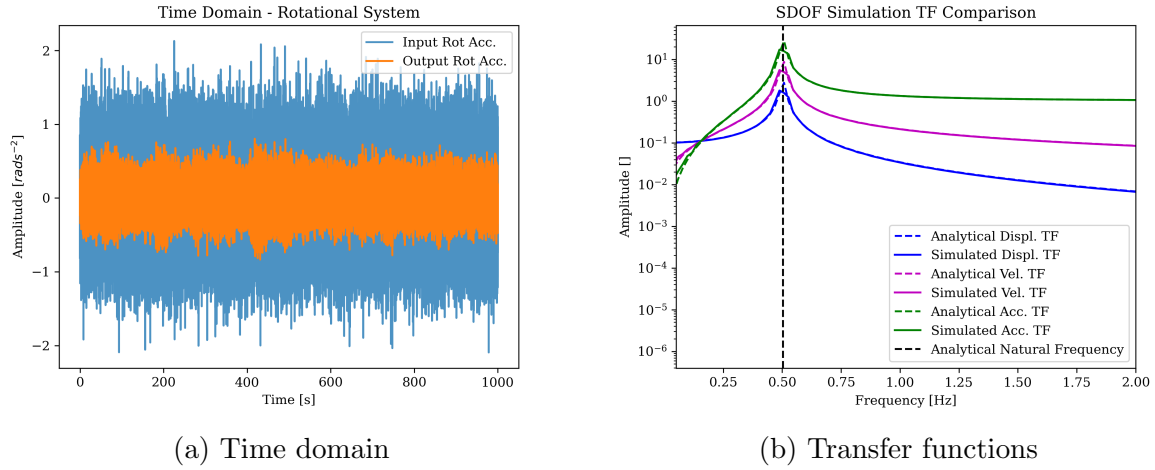


Figure 28: The input and output of a time-domain simulated single-degree-of-freedom (a) and the resulting transfer functions compared with their analytical forms (b)

$$H(\omega) = \frac{S_{zy}(\omega)}{S_{zz}(\omega)} \quad (20)$$

Figure 28A illustrates the broadband white noise acceleration input and resulting acceleration output of a time-domain simulation of the system. Using the definition of the system in terms of its cross-spectral power densities given in Equation 20, the transfer function of the system can be calculated. Figure 28B shows the transfer functions of the system, compared with the analytical cases, showing a high level of agreement between the results from the simulated time-domain system and the analytical system as expected.

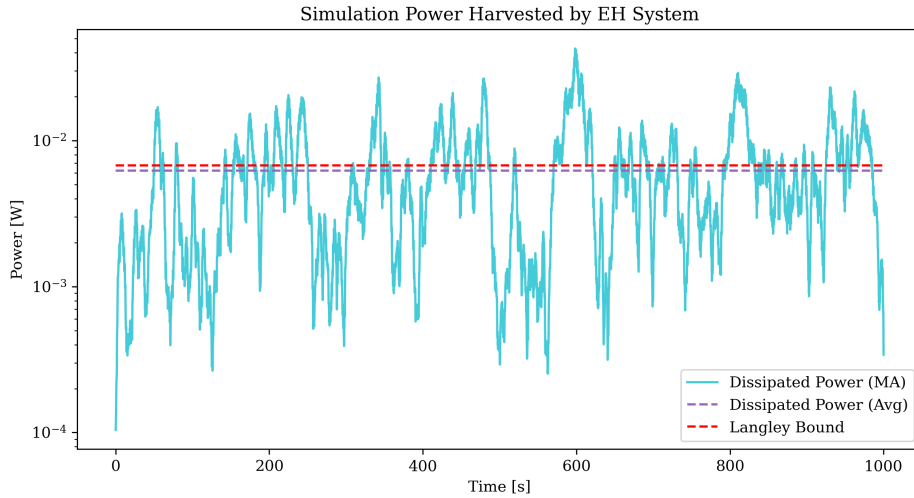


Figure 29: The moving-average power output of the simulation system over time, and the average power compared with the Langley bound.

Figure 29 uses the simulated input and output velocities with Rayleigh's equation in the time domain to calculate the instantaneous power output of the system as a function of time. A moving average is applied due to the high resolution of the data, and the

average power output over the entire simulation is compared with the Langley bound for the system. The results show that the system is operating at an average power output close to the Langley bound, and whilst it can exceed this bound for a period, the average is less than it. Taking an ensemble of simulations shows the same result that Langley's bound on the expected power output of the system is not exceeded for a simple single-degree-of-freedom system.

5.2 Multi-degree-of-freedom systems

$$\mathbf{M}\ddot{\mathbf{y}}_{n+1} + \mathbf{C}\dot{\mathbf{y}}_{n+1} + \mathbf{K}\mathbf{y}_{n+1} = \mathbf{f}_{n+1} \quad (21)$$

Having developed the time-domain simulation for a single-degree-of-freedom system, the simulation was extended to a multi-degree-of-freedom system by using the Newmark-Beta scheme in matrix form, given in Equation 21, alongside Equation 19.

For the multi-degree-of-freedom system, the column vector time history of the forcing input for each degree of freedom is assembled into a single input matrix, and the Newmark-Beta scheme solves for the output time histories for each of the degrees of freedom. The output can then be processed in the same way to determine the frequency response of the system, and the power output of the system over time.

Section 3.3 describes the bandpass effect of a periodic multi-degree-of-freedom system, and a multi-degree-of-freedom simulation is used as an example. The scheme generalises for degree N , and subjecting each degree of freedom to a narrowband Gaussian input before calculating the transfer functions with respect to an arbitrary degree of freedom allows for the bandpass effect to be observed as shown in Figure 7.

5.3 Time and frequency domain comparison

For linear systems, frequency-domain behaviour can be calculated directly in the frequency domain. In this case, the eigenvalues of the system can be calculated using the state space transfer function matrix \mathbf{A} , given in Equation 14, and are equal to the squared natural frequencies of the system. The eigenvectors of the system are the orthogonal mode shapes of the system, and the response of the system is a linear combination of these. Both can be used to calculate the displacement transfer function of the system (where $u_n(x_k)$ is the amplitude of mode n at location x_k) using:

$$H(x_1, x_2, \omega) = \frac{y}{F} = \sum_n \frac{u_n(x_1)u_n(x_2)}{\omega_n^2 - \omega^2 + 2i\zeta\omega_n\omega} \quad (22)$$

Comparison of the time-domain and frequency-domain results, as seen in Figure 28B showed agreement between the two and validated their use for comparison with the experimental results. For a linear system, calculation in the frequency domain is far more efficient, but a nonlinear system requires time-domain results analysis. The results from the experimental work in Section 4.6 showed the system to be weakly nonlinear which will be taken to be approximately linear. Therefore, both methods can be used to model the practical system, although care must be taken with the linearisation assumed.

6 Model verification

Having carried out both experimental and simulation work, the results from each were compared to ascertain the validity of the model used. Once the model has been verified, the results of the experimental work can be incorporated into the simulation which can be used to predict the performance of a multi-degree-of-freedom system, and to inform the design of a practical energy harvesting system that includes a rotational input.

6.1 Piezoelectric calibration

The observation that the relationship between the piezoelectric module's tip acceleration and its voltage output was linear within the operating range was made in Section 4.5. Therefore, further analysis of transfer function G_{34} was carried out to determine the linear relationship in order to calibrate the piezoelectric behaviour of the numerical module. Such a calibration is necessary to calculate the expected voltage output for a simulated acceleration input, and then to simulate the output power of the system for comparison with the experimental case.

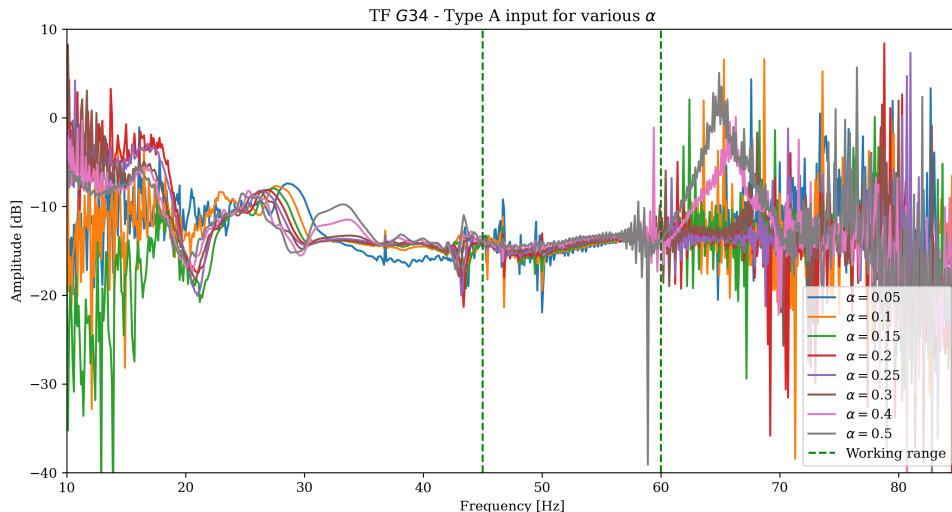


Figure 30: The transfer function between the cantilever tip acceleration in the x direction and the output voltage of the piezo module, G_{34} , for the frequency range of the 10 to 85 Hz input sweep for a range of amplitudes α .

Figure 30 shows G_{34} for the excited frequency range for a range of input amplitudes α . From the plot, the approximately linear relationship between the tip acceleration and voltage can be seen, particularly in the aforementioned operating range of 45 to 65 Hz. The behaviour of the system is less clear above 60 Hz, so the *working range* of the harvester was limited to 45 to 60 Hz. Therefore, a constant β can be used to describe the acceleration-voltage relationship, which is determined by fitting to G_{34} for each of the three input types.

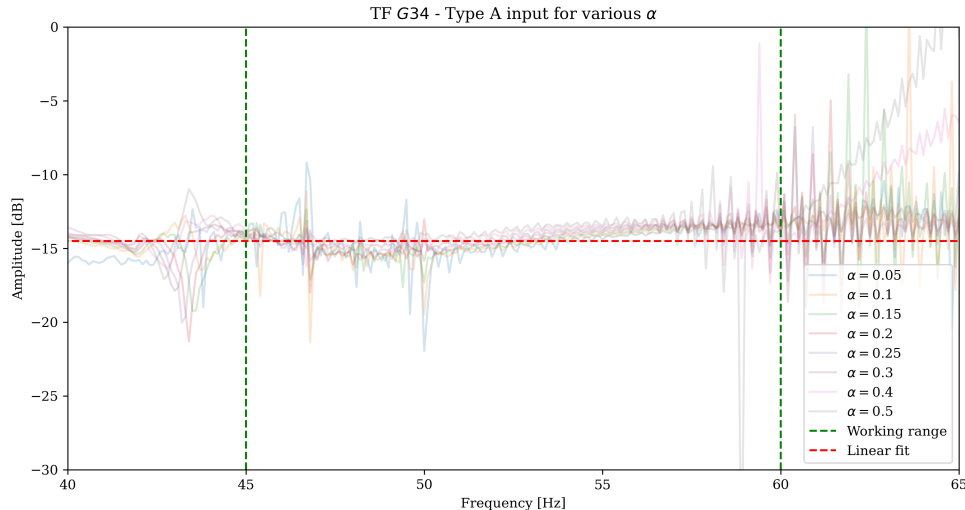


Figure 31: The transfer function G_{34} for the Type A translational input, with a linear fit β showing good agreement in the operating range.

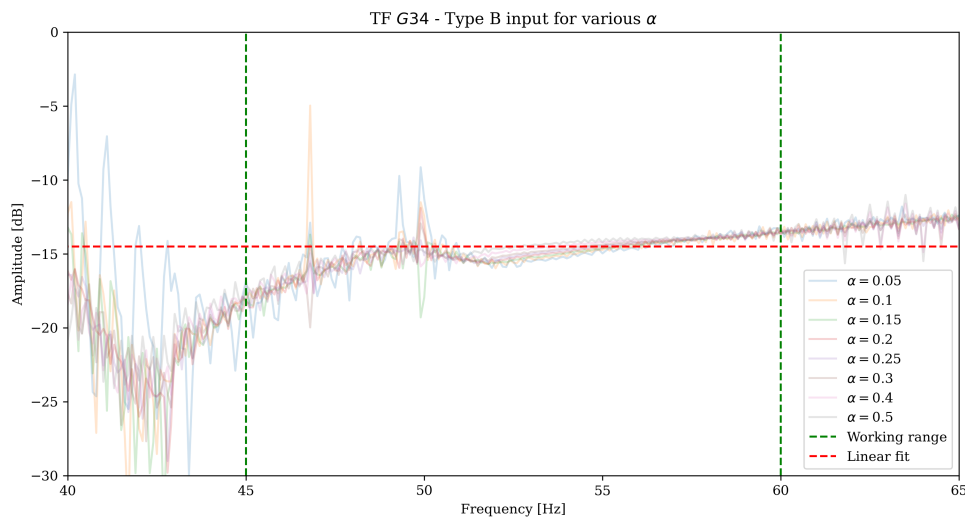


Figure 32: The transfer function G_{34} for the Type B rotational input, with a linear fit β showing reasonable agreement in the operating range.

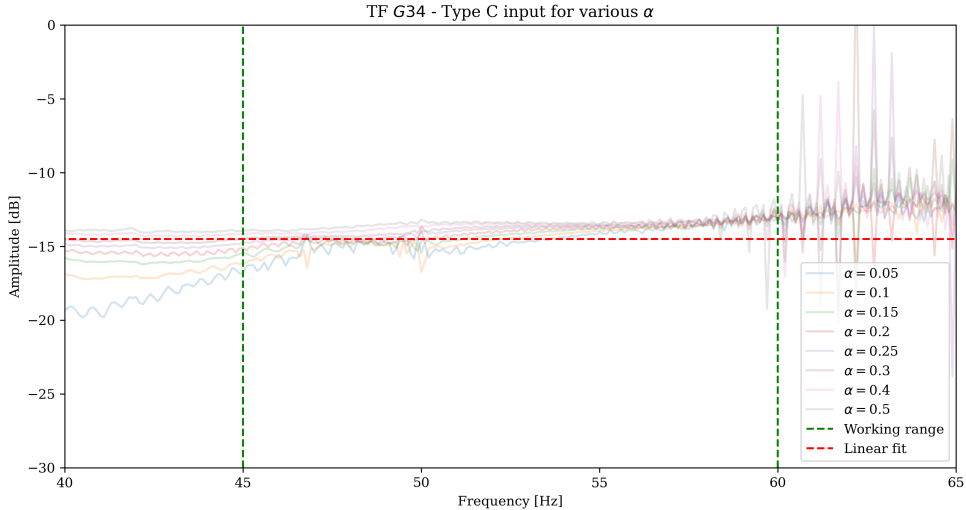


Figure 33: The transfer function G_{34} for the Type C combination input, with a linear fit β showing good agreement in the operating range.

Figures 31, 32, and 33 show the transfer function G_{34} in the working range for input types A, B, and C respectively. A linear fit was carried out across all three input types for all input amplitudes, resulting in a single value of β in dB equal to -14.5 dB. Therefore, the calibration constant is given by:

$$\beta = 10^{\frac{-14.5}{20}} = 0.1884 \quad (23)$$

This calibration constant appeared to give a good fit to the experimental data across the working frequency range, but the true experimental behaviour is not entirely linear. This is most evident in the lower frequency portion of the Type B fit in Figure 32, however, the fit serves as a good approximation for the purposes of the numerical model. As discussed, a more complex piezoelectric model could be used to better represent the behaviour of the system, particularly when scaling the system, but for the purposes of this project, this simpler fit is sufficient.

6.2 Parameter fitting

From the simplified model presented in Section 3.2, the equation of motion for the damped single-degree-of-freedom system is given by:

$$m\ddot{y} + c\dot{y} + ky = c\dot{z} + kz = c(\dot{x} + L\dot{\theta}) + k(x + L\theta) \quad (24)$$

Taking the Laplace transform of Equation 24 gives the transfer functions of the system in terms of both its translational and rotational inputs:

$$G_t(i\omega) = \frac{\bar{y}(i\omega)}{\bar{x}(i\omega)} = \frac{k + i\omega c}{k - m\omega^2 + i\omega c} = \frac{\omega_n^2 + 2i\zeta_n\omega_n\omega}{\omega_n^2 - \omega^2 + 2i\zeta_n\omega_n\omega} \quad (25)$$

$$G_r(i\omega) = \frac{\bar{y}(i\omega)}{\bar{\theta}(i\omega)} = \frac{L(k + i\omega c)}{k - m\omega^2 + i\omega c} = LG_t(i\omega) \quad (26)$$

Typically, a modal circle fit can then be used to determine the parameters of the system. The complex transfer function of the system can be fitted with a circle on a Nyquist plot (real versus imaginary parts of the transfer function), yielding the natural frequency, modal amplitude, and damping ratio.

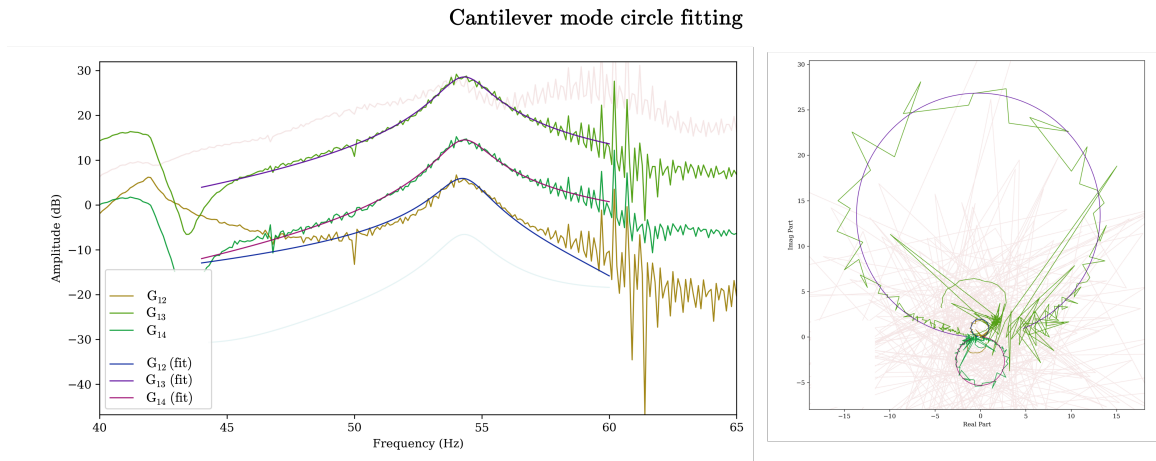


Figure 34: Plots showing the circle fitting to the experimental transfer functions for Type A input with $\alpha = 0.2$ in *pydvma*.

From Figure 34, the parameters (the modal amplitude a_n , the natural frequency ω_n , and the damping ratio, ζ_n) of the cantilever mode can be found for each of the system transfer functions. As discussed, the piezoelectric calibration constant β can be used to show that $G_{14} = \beta G_{13}$. The fits appear to show good agreement with the experimental data in the working range despite the influence of experimental noise.

$$\omega_n = \frac{\omega_d}{\sqrt{1 - \zeta^2}} = \sqrt{\frac{k}{m}} \quad (27)$$

$$\zeta = \frac{c}{2\sqrt{km}} = \frac{1}{2} \left(\frac{c}{k} \right) \cdot \sqrt{\frac{k}{m}} = \frac{1}{2} \left(\frac{c}{k} \right) \cdot \omega_n \quad (28)$$

These parameters allow the damped natural frequency ω_d and damping ratio ζ of the cantilever mode can be found. For simulation of the practical system, the effective mass m , stiffness k , and damping c of the cantilever are required. Ratios of these parameters can be found using the relationships in Equations 27 and 28.

Therefore the fitted parameters for the cantilever must include the ratio between the damping and stiffness, $\frac{c}{k} = 2\frac{\zeta_n}{\omega_n}$, and the natural frequency ω_n , as there is insufficient information to solve for the three unknowns. Substituting these into the numerical system

model allows comparison. The power output of the system can then be simulated using the piezo coefficient β which describes the linear relationship between the output voltage and the cantilever tip acceleration.

Table 6: Summary of the parameters obtained from the circle fits, and the calculated simulation parameters for each of the three input types (m arbitrarily set to 1).

	Type A	Type B	Type C
f_n [Hz]	54.29	56.79	50.64
ω_n [rad s ⁻¹]	341.11	356.82	318.18
ζ_n	0.0163	0.0132	0.0312
$\frac{c}{k}$	$9.56 \cdot 10^{-5}$	$7.40 \cdot 10^{-5}$	$1.96 \cdot 10^{-4}$
m	1	1	1
k	116359	127322	101239
c	11.12	9.42	19.85

6.3 Comparison of simulated and experimental results

Having obtained parameter fits for the system, the experimental data can now inform the numerical model to predict the performance of the harvesting system for each of its input types. Two versions of the numerical model are used: one in the time domain using the model described in Section 5.1, and the other in the frequency domain using the analytical transfer function in Equation 25. The models should match the behaviour of the experimental cantilever when it acts as a single-degree-of-freedom system in the harvesting working range.

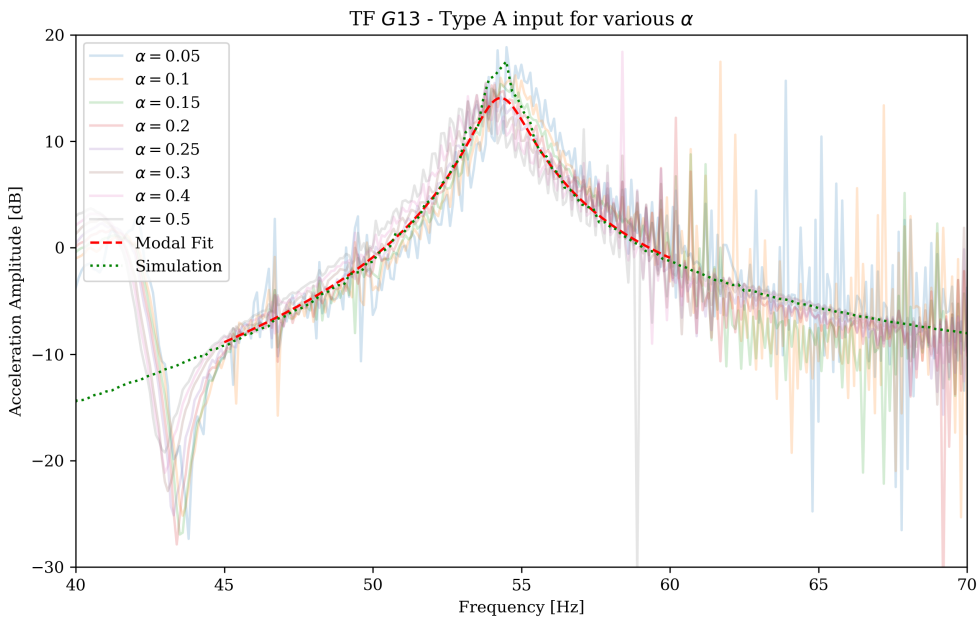


Figure 35: Comparison of the experimental (for a range of α), analytical, and time-domain-simulated transfer functions for the Type A translational input.

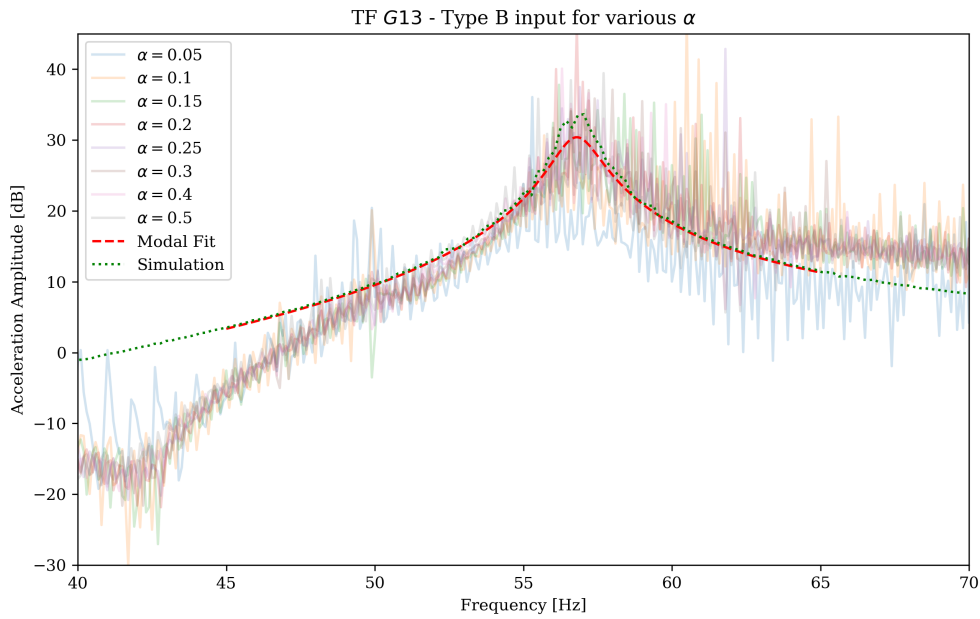


Figure 36: Comparison of the experimental (for a range of α), analytical, and time-domain-simulated transfer functions for the Type B rotational input.

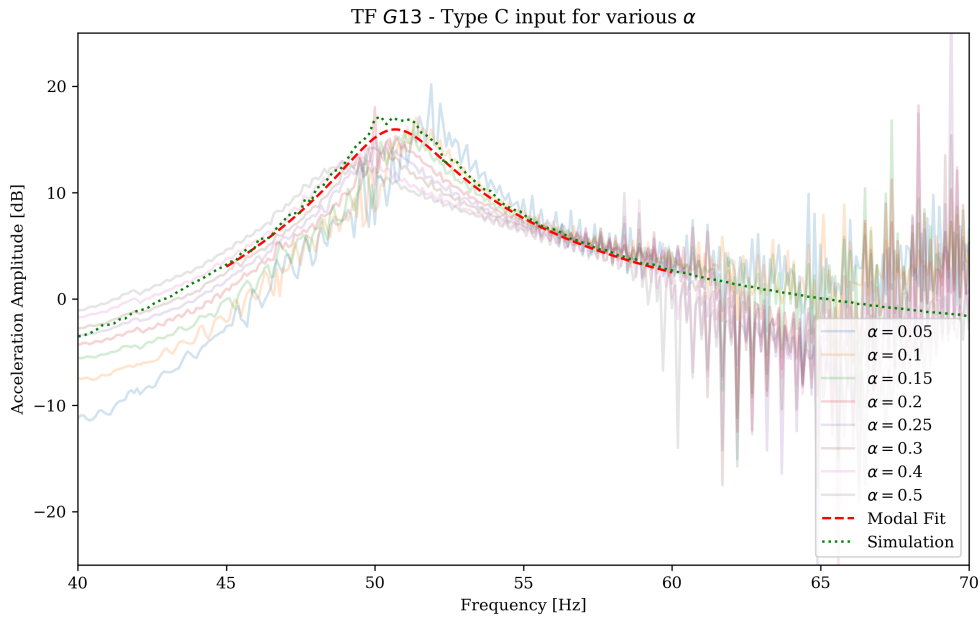


Figure 37: Comparison of the experimental (for a range of α), fitted, theoretical and time-domain-simulated transfer functions for the Type C combined input.

Figures 35, 36, and 37 show the comparison of the experimental, analytical, and time-domain-simulated transfer functions for each of the input types. The analytical transfer function fits are limited to the working range, whilst the time-domain simulation is

carried out across the full frequency range, but only valid for the single-degree-of-freedom harvesting region.

In general, all three datasets show good agreement within the working range, despite the presence of experimental noise and the weak softening nonlinearity of the system. Type A and Type C inputs show particularly good agreement, whilst the Type B input shows some deviation.

This is likely due to the lower signal-to-noise ratio and lower overall data quality, but the mismatch in the shape would suggest that the system is not entirely due to a single degree of freedom in this region. Such behaviour is not captured by the two models, and so the prediction of the system's performance in rotation is less accurate. The misalignment appears to be a clockwise rotation of the transfer function, which is typically due to a missing factor of ω in the numerator; this would imply that the purely rotational transfer function does not follow the form given in Equation 26, despite it being calculated between input acceleration and output acceleration. Instead, it would imply that this has some frequency dependence:

$$G_r(i\omega) = g(L, \omega) \cdot G_t(i\omega) \quad (29)$$

Where $g(L, \omega)$ is some frequency and inertia dependent function. Providing an improved rotational model of the system would significantly improve the accuracy of the simulation results, but the current model is sufficient at the peak response. This is the vital region for calculating the peak power output of the system, and so comparisons between input Types A, B, and C are still valid.

Having validated the numerical models against the experimental results, the power output of the system can be calculated for each of the input types using the piezoelectric calibration constant β . This results in a model of the specific system in the frequency range that allows for the prediction of the maximum power output for each of the input types.

7 Conclusions

Having started with the broad aim of ‘pushing the bounds of energy harvesting’, the project has been successful in demonstrating that a method outside of the conditions of Langley’s bound has the potential to improve the performance of an energy harvesting system.

A model has been developed for a single-degree-of-freedom system subject to both translational and rotational input, and the results of the experimental work show good agreement with the simulation. This model has been used to predict the performance of the system for a range of input types and compared with experimental measurements. From this, the model can be used to predict the power output for more complex multi-degree-of-freedom systems at different scales, providing a powerful tool for harvesting system design.

Whilst a representative combination input (‘Type C’) was used to attempt to show the benefits of such a system, the experimental results proved inconclusive. For the specific rig, it would appear that the balance of rotation and translation in the input mix affects the performance of the system, as does the practical constraints applied by a real-world dual input system. Therefore, further work is required to characterise the combined input and its effect on the system’s performance.

Consequently, in relation to the objectives set out in Section 1.2 it can be concluded that:

1. The simplified theoretical model presented for the system shows good agreement with the experimental results for the single-degree-of-freedom system, and can be used to predict the performance of the system for a range of input types.
2. The experimental rig designed and built for the project was able to successfully supply translational and rotational inputs to the system, as well as a representative combined input.
3. The numerical model developed for the system showed agreement with the analytical results expected for both single and multi-degree-of-freedom systems.
4. The experimental results validated the numerical model, and allowed the prediction of the power output for a wide range of simulated systems.
5. Rotational inputs have the potential to improve the power output of a system, but the experimental results showed that the composition of a combined input can have a significant effect on the performance of the system and requires further work.

7.1 Recommendations for future work

A number of recommendations for future work have been made throughout the project, in addition to the possibility of exploring the other circumvention methods that were not pursued.

As mentioned, the most significant of these is the characterisation of the combined ‘Type C’ input. Such an input mode was intended to show the representative performance of a system subject to both rotation and translation, but the results of the experimental work in Section 4.7 showed a decrease in power output compared to its individual components. This was attributed to the phase relationship between the two shakers, and so a future experiment could involve use of balanced shakers with a variable phase shift between them to ascertain the effect of the composition of a combined input on the harvesting performance of the system. Alternatively, separate, uncorrelated narrowband white noise inputs could be used whereby the phase is not a parameter like it is with harmonic inputs.

The aim of these additional experiments would be to better understand the relationship between the input composition (in terms of its translational and rotational components) and the power output of the system. This would allow for the design optimisation for a specific input, to maximise the power output of the system. For example, a certain location in the body may have a higher proportion of rotational motion, and so ideally the harvester could be tailored to its input spectrum, yielding further improved performance.

Additionally, the true behaviour of the scaling arguments used requires further investigation. The simple approach used was sufficient for the scope of this project, but in order to fully validate the application of the results to a smaller scale multi-degree-of-freedom device, further work is needed. This would include a more sophisticated piezoelectric model to represent the transduction behaviour at a smaller scale. Furthermore, practical verification of the bandpass theory discussed would be required to ensure that the multi-degree-of-freedom model is valid. This further work would ensure that the predicted power output of the numerical model for smaller and more complex systems is accurate, which is vital for practical application.

8 References

- [1] R. Langley, “A general mass law for broadband energy harvesting,” *Journal of Sound and Vibration*, vol. 333, pp. 927–936, 2 2014.
- [2] L. Dong, A. B. Closson, C. Jin, I. Trase, Z. Chen, and J. X. Zhang, “Vibration-energy-harvesting system: Transduction mechanisms, frequency tuning techniques, and biomechanical applications,” 10 2019.
- [3] P. Pillatsch, E. M. Yeatman, and A. S. Holmes, “A piezoelectric frequency up-converting energy harvester with rotating proof mass for human body applications,” *Sensors and Actuators, A: Physical*, vol. 206, pp. 178–185, 2 2014.
- [4] F. U. Khan and I. Ahmad, “Review of energy harvesters utilizing bridge vibrations,” *Shock and Vibration*, vol. 2016, 2016.
- [5] S. Roy, A. N. W. Azad, S. Baidya, M. K. Alam, and F. Khan, “Powering solutions for biomedical sensors and implants inside the human body: A comprehensive review on energy harvesting units, energy storage, and wireless power transfer techniques,” *IEEE Transactions on Power Electronics*, vol. 37, pp. 12237–12263, 10 2022.
- [6] M. F. Daqaq, R. Masana, A. Erturk, and D. D. Quinn, “On the role of nonlinearities in vibratory energy harvesting: A critical review and discussion,” 2014.
- [7] Y. Jia and A. A. Seshia, “Power optimization by mass tuning for mems piezoelectric cantilever vibration energy harvesting,” *Journal of Microelectromechanical Systems*, vol. 25, pp. 108–117, 2 2016.
- [8] D. E. Newland, *An Introduction to Random Vibrations, Spectral and Wavelet Analysis : Third Edition*. Dover Civil and Mechanical Engineering, 2012.
- [9] R. S. Langley, “Bounds on the vibrational energy that can be harvested from random base motion,” *Journal of Sound and Vibration*, vol. 339, 2015.
- [10] C. Meinhardt, D. Newland, J. Talbot, and D. Taylor, “Vibration performance of london’s millennium footbridge,” 2017.
- [11] M. A. Karami and D. J. Inman, “Linear and nonlinear energy harvesters for powering pacemakers from heart beat vibrations,” vol. 7977, p. 797703, SPIE, 3 2011.
- [12] H. J. Xiang, Z. F. Shi, S. J. Wang, and Y. L. Mo, “Periodic materials-based vibration attenuation in layered foundations: Experimental validation,” *Smart Materials and Structures*, vol. 21, 11 2012.
- [13] D. E. Newland, *Mechanical Vibration Analysis and Computation*. 2013.
- [14] T. Butlin, “pydyma 0.9.8, a python package for dynamics and vibration measurements and analysis,” 2024. [Online; accessed 23-May-2024].
- [15] piezo.com, “Piezoelectric bending transducer (s233-h5fr-1107xb),” 2024. [Online; accessed 23-May-2024].
- [16] N. M. Newmark, “A method of computation for structural dynamics,” *Journal of the Engineering Mechanics Division*, vol. 85, no. 3, pp. 67–94, 1959.

Appendix

A Risk assessment retrospective

At the start of the project, an initial hazard assessment was carried out, identifying potential risk associated with the practical aspects carried out later in the year. The only other risk of note was the use of Display Screen Equipment (DSE), and guidance was followed on safe computer working throughout the project.

Table 7: The risk assessment carried out for the project experimental work.

Hazard	Effect	Control Measures	Risk
Injury due to detached components	Parts may become loose during vibration testing and cause injury	Ensure that all components are sufficiently fastened before testing, and limit amplitude for shake input. Wear safety glasses for any higher amplitude testing if required, but testing will not be carried out to failure	Low
Heavy components	Heavy components (amplifiers, tables, clamps) may cause injury when lifting or if dropped	Ask for assistance when carrying larger items, ensure closed footwear is worn	Low
Electrocution	Piezoelectric components may output tens of volts	Ensure that the load is electrically connected securely, and that resistances are sufficient to limit the voltage output	Low

Table 7 details the risk assessment carried out following the planning of the experimental work in the Lent term. The hazards identified were injury due to component detachment, heavy components, and the risk of electrocution.

In retrospect, no heavy components were required, and so this hazard was not present as initially thought. The electrocution hazard was also low following the choice of the piezoelectric component which output less than 10 V peak, but care was still taken. The rig was also not driven to severe amplitudes, and its fixings were well secured and regularly checked, and so the risk of injury due to detached components was also very low.

Therefore, the risk assessment reflected the hazards encountered well, and if the project was to be carried out again, the same assessment would be used. The only adjustments that might be required are additional measures for larger amplitude testing, but this is dependent on the design of the rig and the tests carried out - this was not required for the scope of this project.